Physical conditions, structure and dynamics of a zoned magma chamber: Mount Pelée (Martinique, Lesser Antilles arc).

Michel Pichavant, Caroline Martel, Jean-Louis Bourdier, Bruno Scaillet

Physical conditions, structure, and dynamics of a zoned magma chamber: Mount Pelée (Martinique, Lesser Antilles Arc)

Michel Pichavant
Institut des Sciences de la Terre (ISTO), Orléans, France

Caroline Martel
Bayerisches Geoinstitut, Universität Bayreuth, Bayreuth, Germany
Institut des Sciences de la Terre (ISTO), Orléans, France

Jean-Louis Bourdier and Bruno Scaillet
Institut des Sciences de la Terre (ISTO), Orléans, France

Received 24 January 2000; revised 20 November 2000; accepted 19 August 2001; published 18 May 2002.

[1] Experimental results and petrologic observations of the eruptive history of Mount Pelée are integrated, and a model for the magma storage system is presented. Recent (stage 3) Plinian and Pelean activity (P1, 650 years B.P.; 1902, 1929) erupted relatively homogeneous andesites (average 62 wt % SiO_2). They are porphyritic (35–58 vol % crystals) and contain phenocrysts of plagioclase (Plag) (An_{50-90}), orthopyroxene (Opx) (En_{52-60}), and magnetite (Mt) ($\sim Mt_{70}$). Glasses (both interstitial and trapped) are rhyolitic (74–77 wt % SiO_2). Clinopyroxene (Cpx), ilmenite (Ilm), amphibole (Amph) (mostly resorbed pargasitic hornblendes), and olivine (Ol) are present as minor phases. Products of 1902 and 1929 contain mafic enclaves (51–59 wt % SiO_2) with compositions similar to basaltic andesite lavas erupted during stage 2 (40,000–19,500 years B.P.). Conditions in the andesitic part of the magma chamber, as determined from experimental phase equilibria, do not differ between the P1, 1902, and 1929 eruptions (875–900°C, 2 ± 0.5 kbar, ΔNNO = +0.4–0.8, melt H_2O content of 5.3–6.3 wt %). New experimental data on a basaltic andesite composition (53 wt % SiO_2) from stage 2, at 4 kbar, 950–1025°C, for melt H_2O concentrations from 8.3 to 2.6 wt %, and f_{O2} between NNO and NNO + 4 simulate crystallization in the mafic part of the chamber. Liquidus or near-liquidus Ol, An-rich Plag, Al- and Fe^{3+}-rich salite and augite, pargasitic hornblende, and Al- and Mg-rich Mt have compositions close to phenocrysts in mafic products from stages 2 and 3. Experimental liquids range from basaltic andesite to dacite. Application of experimentally derived mineral-melt Al/Si and Fe/Mg partition coefficients to mineral compositions from mafic lavas and cumulates from stage 2 shows that the chamber is fed by relatively evolved parental basaltic liquids (Mg # $\sim$ 55–60)(Mg # = Mg/(Mg + Fe^T). They have low temperatures ($\leq$1050°C), high melt H_2O contents (>5–6 wt %), and f_{O2} (ΔNNO mostly between +1 and +2) and crystallize an Ol + Cpx + Mt assemblage followed by Plag + Amph, although Amph may have started to crystallize with Ol and Cpx. Compositions of natural glasses and amphibole in mafic cumulates and lavas record a continuous evolution from basaltic-basaltic andesite to basaltic andesite-dacite liquids. Crystal fractionation of basaltic magmas is the main process controlling the chemical diversity at Mount Pelée. Crystallization in the mafic part produces an andesitic-dacitic residual liquid which subsequently evolves to produce the andesitic part. The present-day situation is typical of low fluxes of mafic magmas in comparison with stage 2. *INDEX TERMS:* 3630 Mineralogy and Petrology: Experimental mineralogy and petrology; 8439 Volcanology: Physics and chemistry of magma bodies; 8414 Volcanology: Eruption mechanisms; *KEYWORDS:* basalt, andesite, volcanism, experiments, magma storage

1. Introduction

[2] Volcanic activity at convergent plate margins and island arcs is typically characterized by a large variety of eruptive styles, from explosive to effusive. For eruption forecasting and evaluation of associated hazards it is crucial to understand the factors that influence eruptive styles and the transition between explosive and effusive eruptions. Although the role of syneruptive degassing at shallow levels is now recognized to be important, there is a general consensus that processes of magma storage at depth strongly influence eruptive styles [e.g., *Eichelberger and Westrich*, 1981; *Fink*, 1983; *Eichelberger et al.*, 1986; *Jaupart and Allègre*, 1991; *Villemant and Boudon*, 1998]. Modeling magma storage in subvolcanic reservoirs requires, in a first step, the melt H_2O concentration, T, P, f_{O2} to be determined because these parameters control the physical and chemical properties of the magma body. Several recent studies have demonstrated the great potential of the experimental approach for the precise determination of preeruptive parameters at active arc volcanoes [*Rutherford et al.*, 1985;

0148-0227/02/2001JB000315$09.00

Rutherford and Devine, 1988, 1996; *Gardner*, 1995; *Barclay et al.*, 1998; *Martel et al.*, 1998; *Scaillet and Evans*, 1999]. In a second step a dynamic picture of the magma reservoir and of its evolution with time is needed. This requires interpreting information on the eruptive history of the volcano in the light of the available experimental or theoretical constraints. Studies of compositional zonations that characterize eruption products of many arc volcanoes are especially critical since their interpretation provides direct inferences on the structure, geometry, and dynamics of the magma reservoir [e.g., *Hildreth*, 1981; *Eichelberger et al.*, 2000].

[3] In the present study, we focus on Mount Pelée (Martinique, Lesser Antilles arc). Recent activity of this andesitic volcano includes both Plinian and Pelean (dome-forming) eruptions [*Lacroix*, 1904; *Boudon and Gourgaud*, 1989; *Smith and Roobol*, 1990]. *Martel et al.* [1998] compared phenocryst rim and glass compositions from recent eruptions with compositions from Mount Pelée andesite experimental products. They emphasized the lack of variation in the physical and chemical conditions of magma storage preceding the recent eruptions and stressed the bulk chemical homogeneity of the tapped andesitic magma body. Yet the occurrence of mafic lavas, mafic enclaves, and mingled/mixed products in the eruptive history of the volcano [*Bourdier et al.*, 1985; *Fichaut et al.*, 1989a, 1989b; *Gourgaud et al.*, 1989] demonstrates that magma storage at Mount Pelée needs to be placed in the broader context of an open, compositionally zoned igneous system [e.g., *Hildreth*, 1981; *Bacon*, 1986]. It is therefore critical to impose precise physical and chemical constraints on the mafic magmas, as well as on the andesitic magmas. Understanding the relationships between the various residing magmas (including the question of the origin of the andesites) is also necessary for a realistic modeling of the structure and dynamics of the magma system. This paper integrates experimental results with petrologic observations of the eruptive history of Mount Pelée, and a model for the magma storage system is presented. New experimental data are reported on a basaltic andesite representative of the mafic magmas, and new petrographical, geochemical, and mineralogical data are given for several eruptions. This new information is combined with previously published studies, including the recent experimental work on Mount Pelée andesites by *Martel et al.* [1999].

[4] In the following, the terms ''magma storage system,'' ''magma reservoir,'' and ''magma chamber'' will be used interchangeably to designate the source of magma, whether composed of a single physically continuous reservoir [*Bacon*, 1986] or of two physically discontinuous, vertically superimposed communicating reservoirs [*Hildreth*, 1981; *Fichaut et al.*, 1989a]. In either case, the magma reservoir may comprise chemically homogeneous or subhomogeneous units that will be hereinafter designated as ''parts'' or ''bodies'' (e.g., the ''andesitic body'' of the magma chamber). In this paper, compositional zonation is considered at the scale of the magma storage system taken as a whole, whether physically continuous or discontinuous.

2. Volcanological Background

[5] The geology of Mount Pelée has been extensively studied over the past 25 years. Our current knowledge is mainly based on a geological map at 1/20,000 scale [*Westercamp and Traineau*, 1983a] and an extensive set of stratigraphic sections and ^{14}C dates [*Roobol and Smith*, 1976; *Westercamp and Traineau*, 1983b; *Traineau et al.*, 1989; *Smith and Roobol*, 1990]. The volcano's history is conveniently divided into three periods [*Westercamp and Traineau*, 1983b; *Bourdier et al.*, 1985]. During the first period (stage 1) an ancestral volcano formed whose size and summit position were roughly those of the present day (Paleo-Pelée of *Vincent et al.* [1989]). The remnants of this are mostly lithified pyroclastic and epiclastic breccias; the few lava flows occurring on the upper flanks all belong also to the primitive volcano. The age of Paleo-Pelée remains poorly constrained. It is younger than the neighboring Mount Conil (one K-Ar date at 0.6 ± 0.1 Ma [*Nagle et al.*, 1976]), and a single K-Ar age on a Paleo-Pelée breccia is 0.4 ± 0.2 Ma [*Bellon et al.*, 1974]. The second period (stage 2, from 40,000 to ~19,500 years B.P. [*Westercamp and Traineau*, 1983b]) was dominated by pyroclastic ash-and-scoria flows of more mafic composition (basaltic andesite) than the Paleo-Pelée lavas (St. Vincent stage of *Vincent et al.* [1989]). A sectorial collapse affected the southwest flank of the volcano during this stage [*Vincent et al.*, 1989], forming a large (6 × 2.5 km) morphostructural feature of the volcano which has been a major control on the distribution of later eruptive products. The third period (stage 3) is currently defined as spanning from ~13,500 years B.P. to present, the volcano having been apparently quiet (no ^{14}C date) between ~19,500 and ~13,500 years B.P. [*Westercamp and Traineau*, 1983b]. Products from this period are almost exclusively either Plinian (pumice fallout and ash-and-pumice flow) or Pelean (block-and-ash flow and lithic surge) deposits of dominantly silicic andesite composition. In the best documented last 5000 years, 6 Plinian and 12 Pelean eruptions have been identified [*Westercamp and Traineau*, 1983b; *Smith and Roobol*, 1990]. The recent activity of Mount Pelée thus displays a pattern of eruptive styles alternating from explosive Plinian eruptions of rather constant magnitude (typically VEI 4) to extrusive dome-forming eruptions [*Roobol and Smith*, 1976; *Westercamp and Traineau*, 1983b; *Smith and Roobol*, 1990; *Boudon et al.*, 1994]. A prominent feature of Mount Pelée activity is that dome-forming eruptions may involve major hazards because of the possibility of highly energetic pyroclastic flows, as demonstrated by the high-velocity pyroclastic flow eruptions of May–August 1902 [*Lacroix*, 1904].

3. Methods

3.1. Samples

[6] Eruptions considered in detail in this study include P1 (dated to 650 years B.P.), 1902–1904, and 1929–1932. These eruptions are representative of the recent period of activity of the volcano (stage 3, see section 2). The P1 eruption [*Villemant et al.*, 1996] is the last Plinian event before the cycle of dome-forming eruptions of 1902 and 1929. This eruption is characterized by an initial phase of Pelean activity followed by a Plinian phase. The P1 deposits include basal surges with features similar to the nuée-ardente deposits of May–August 1902 and Plinian fallout and flow deposits. The Plinian deposits lie directly on the surge deposits, and no erosional surface is present, suggesting a time interval of less than a few days between the two eruptive phases. Therefore the P1 eruption offers the opportunity to compare Pelean and Plinian products from the same eruption. The 1902–1904 eruption was first described by *Lacroix* [1904]. More recently, several studies have analyzed the sequence of events preceding the catastrophic eruption of 8 May 1902, established the stratigraphy and characterized the deposits [see *Boudon and Gourgaud*, 1989; *Bourdier et al.*, 1989]. The 1902–1904 eruption of Mount Pelée is the type Pelean eruption. Dome growth is associated with highly explosive activity, leading to laterally directed pyroclastic flows such as the 8 May 1902, surge responsible for the destruction of the town of St. Pierre and the loss of nearly 30,000 lives. Other similar high-energy pyroclastic flows were recorded on 20 and 26 May, 6 June, 9 July, and 30 August 1902, this phase of explosive activity being followed by a more quiescent period of dome and needle growth. The 1929–1932 Pelean eruption, first described by *Perret* [1937], is similar in many aspects to that of 1902–1904. It is, however, characterized by block-and-ash flows of comparatively lower energy and lacked the highly explosive phase typical of the 1902 eruption.

[7] Samples selected for detailed studies come from well-preserved deposits showing unambiguous mechanisms of emplacement (Figure 1). A total of 86 samples have been collected. The P1

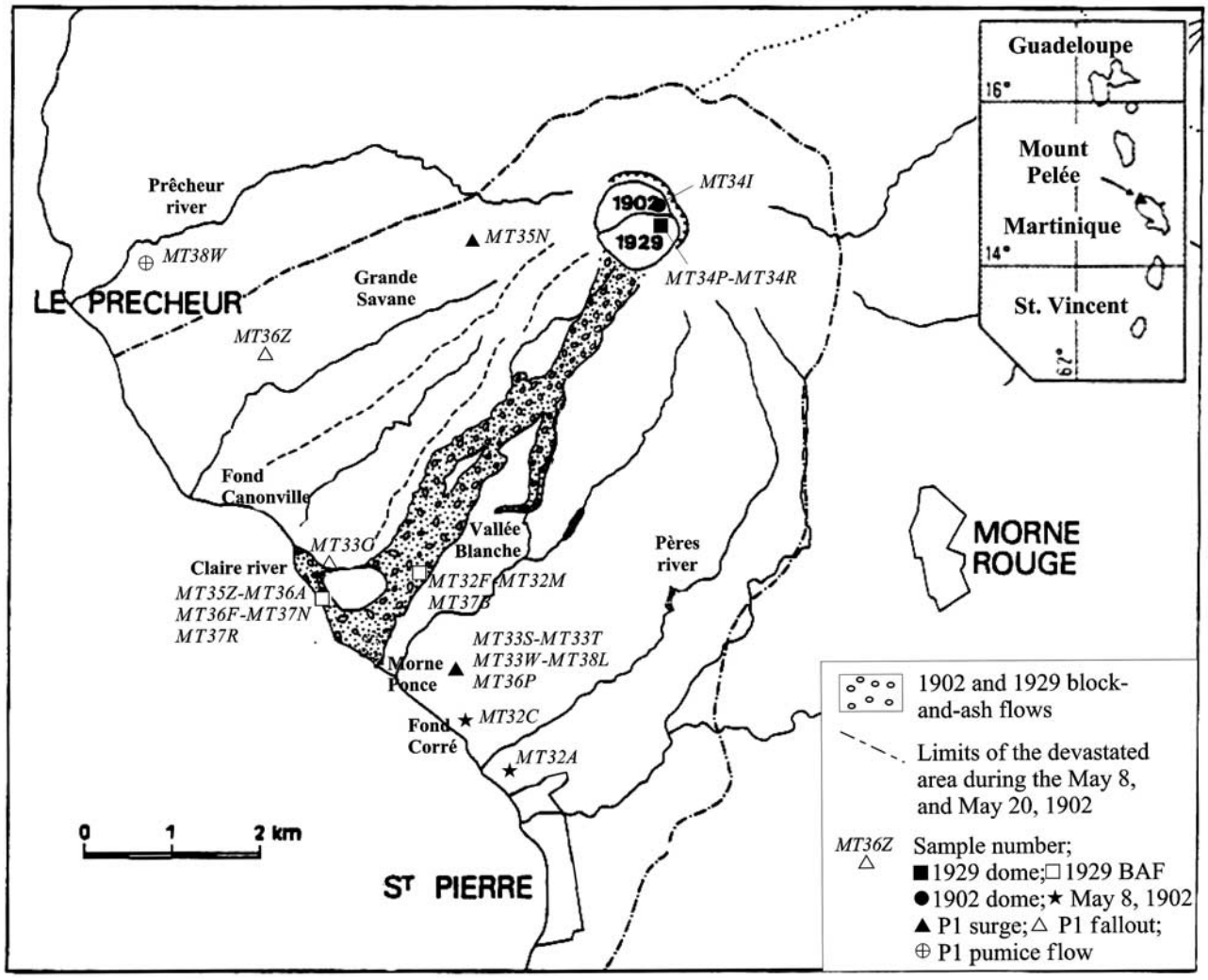

Figure 1. Schematic map of Mount Pelée showing distribution of pyroclastic flows and sampling locations.

samples include the main Pelean basal surge (referred to as P1 surge), and the Plinian fallout and pumice flow (description from *Traineau et al.* [1989]). The 1902–1904 and 1929–1932 samples come from the 1902 and 1929 domes, from the 8 May, 20 May, and 30 August 1902 surges, and from the 1929–1932 block-and-ash flows (hereinafter referred to as 1929 BAF). Samples are divided into three main lithologies depending on their porosity [*Martel et al.*, 2000]: (1) glassy lithic clasts (porosity up to 25 vol % on a crystal-free basis, (2) vesicular lithic clasts (between 25 and 50 vol % porosity) and (3) pumices (>50 vol % porosity). Pelean products (P1 and 8 May 1902 surges, 1902 and 1929 domes, and 1929 BAF) have porosities of 20–40 vol % on average and are mostly vesicular lithic clasts. In the P1 surge, pumices (50–55 vol %) are also present. Plinian products (fallout and pumice flow) from P1 have average porosities of 70–75 vol %. The samples collected are homogeneous and lack textural indications of mingling (e.g., presence of mafic enclaves and droplets and banded textures) such as described by *Gourgaud et al.* [1989] in some 1902 and 1929 rocks.

3.2. Analytical Methods

[8] Whole rock analyses were performed on a few samples and mainly for comparative purposes because a large body of major element data is already available for Mount Pelée [*Bourdier et al.*, 1985; *Fichaut et al.*, 1989a; *Gourgaud et al.*, 1989; *Smith and Roobol*, 1990; *Villemant et al.*, 1996]. Five samples (lithic and pumice clasts from the P1 surge, fallout and pumice flow from the P1 Plinian phase, and 1929 dome) were powdered and analyzed for major elements by inductively coupled plasma-atomic emission spectrometry (ICP-AES) and FeO by titration [*Govindaraju*, 1994].

[9] Petrographic studies were carried out on a total of 44, 10, and 26 samples from the P1, 1902, and 1929 eruptions, respectively, and included a few samples from *Traineau et al.* [1989] (P1) and *Gourgaud et al.* [1989] (1902 and 1929 products). Modal compositions were determined by point counting on one to five thin sections (~1300 points per section) for seven lithological units (P1, surge (distinguishing between lithic and vesicular facies), fallout pumice; 1902, dome, 8 May surge; 1929, dome, block-and-ash flows). Only phases larger than ~100 μm were counted as phenocrysts. Twenty-four samples from the seven units above were selected for detailed mineralogical studies.

[10] Thin sections were examined by scanning electron microscopy (SEM) backscattered electron imaging using a JEOL JSM 6400 microscope operating at 15 kV acceleration voltage. Phenocrysts were analyzed using either a Cameca Camebax microbeam or a Cameca SX 50 electron microprobe. Both point analyses and compositional profiles (plagioclase and orthopyroxene) were

obtained. The analytical conditions were 6 or 12 nA sample current, 15 kV acceleration voltage, focused beam (1–2 μm), and 10 s counting time on peak. Various silicates and oxides were used as standards and either ZAF (atomic number (Z), absorption (A), fluorescence (F)) or PAP (Pouchou and Pichoir) correction procedures were employed, depending on the instrument. Analytical errors are 1% relative for SiO_2 and Al_2O_3; 2% for CaO; 3% for FeO, MgO, and TiO_2; and 5% for MnO, Na_2O, and K_2O. Matrix glasses and glass inclusions were analyzed on the Cameca SX 50 electron microprobe with the same analytical conditions, except for the larger beam size (5 or 10 μm). Alkali migration was corrected by using hydrous, rhyolitic secondary standard glasses of known alkali concentrations, measured by wet chemistry [*Pichavant*, 1987; *Martel et al.*, 1999]. Correction factors varied from 0.95 to 1.2 for Na_2O and from 0.95 to 1.1 for K_2O depending on water content. H_2O concentrations of natural glasses were measured by Fourier transform infrared (FTIR) and with the by-difference method. Analytical details are given by *Martel et al.* [1999].

3.3. Experimental Methods

[11] Experiments were performed both on andesite samples from recent eruptions (stage 3) and on a mafic basaltic andesite from the second period of activity (stage 2), considered to be representative of the mafic magmas present as enclaves in recent eruption products (Figure 2). The three andesites investigated experimentally were selected among samples collected from the P1 and 1929 eruptions. They have whole rock chemistries virtually identical to each other (Table 1 and section 4.1). The basaltic andesite sample is a dark scoria from Grand Rivière, collected and described by *Bourdier et al.* [1985]. This sample was reanalyzed for major elements at Université de Bretagne Occidentale, Brest [*Cotten et al.*, 1995]. Although slightly more mafic compositions exist as enclaves (see Table 1 and Figure 2), the basaltic andesite selected is one of the most mafic lava erupted from Mount Pelée (Mg # = 48.7 with total Fe as FeO, Table 1). The sample is porphyritic and has a total phenocryst content of 34% in volume [*Bourdier et al.*, 1985]. The most abundant phenocryst is plagioclase. Clinopyroxene, orthopyroxene, amphibole, olivine, and magnetite phenocrysts are also present.

[12] Experimental procedures and results for the andesites are detailed elsewhere [*Martel et al.*, 1999]. In this paper, new experimental data are presented for the basaltic andesite. For these, techniques were basically the same as previously employed [*Martel et al.*, 1999] and need only to be recalled here. The powdered basaltic andesite sample was fused in air at 1400°C, 1 atm in Pt capsules. Two cycles of melting of 2–4 hours each, with grinding in between, were performed, yielding an homogeneous glass whose composition was checked by electron microprobe. The glass was then crushed to ~10–50 μm and loaded in Au tubes together with either 15 wt % H_2O for H_2O-saturated experiments or 15 wt % (H_2O + CO_2) for H_2O-undersaturated experiments. The CO_2 source was $Ag_2C_2O_4$. All experiments were of crystallization (i.e., synthesis) type, and they were carried out in an internally heated gas vessel pressurized with Ar-H_2 mixtures for durations ranging between 13 and 99 hours. Ni-Pd-O sensors were used to measure f_{H2}. Oxygen fugacity was calculated from f_{H2} and f_{H2O} and is known to better than 0.25 log unit [*Scaillet et al.*, 1995; *Martel et al.*, 1999]. Seven experiments totaling 20 charges were performed at ~4 (±0.1) kbar, between 950 and 1025 (±5) °C and for ΔNNO values ranging between +0.2 and +3.9. A drop-quench technique modified after *Roux and Lefèvre* [1992] was systematically used, allowing quench rates of ~100°C s^{-1} for all experiments.

[13] Charges were systematically studied by SEM and analyzed by electron microprobe, the analytical procedures being essentially the same as for the natural samples. For the electron microprobe analysis of experimental glasses, a sample current of 6 nA and beam sizes between 5 and 15 μm (depending on the proportion of crystals present in the charge) were used. In addition, basaltic andesite secondary standard glasses (starting glasses and hydrous glasses from charges HAB17 and HAB18) were analyzed together with experimental glasses to correct for alkali migration and to estimate glass H_2O contents with the by-difference method (see below and *Martel et al.* [1999]). Mass balance calculations were

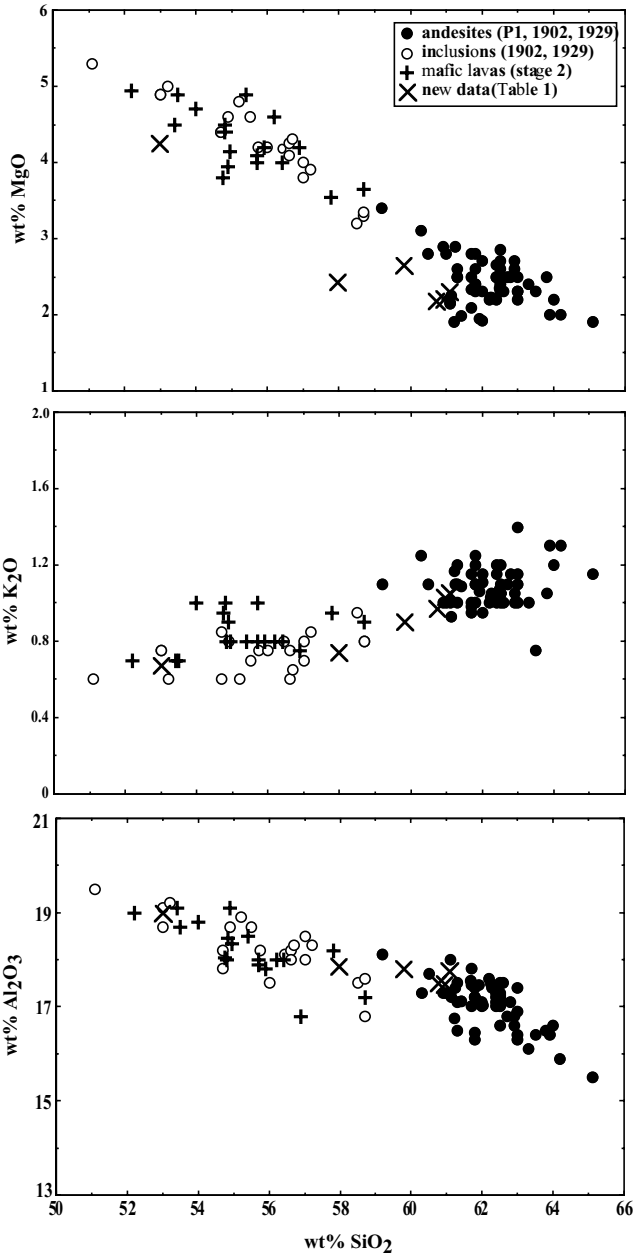

Figure 2. Major element variation diagrams for andesites and mafic enclaves and for mafic lavas from the third and second stages of activity of Mount Pelée, respectively. Sources of data are for andesites and mafic enclaves from the third stage, *Fichaut et al.* [1989a], *Gourgaud et al.* [1989], and *Smith and Roobol* [1990] and for mafic lavas from the second stage, *Bourdier et al.* [1985]. The new analyses (five andesites from P1 and one mafic lava) are shown as crosses. Note the overlap in composition between the mafic lavas of the second stage and the mafic enclaves of the third (recent) period.

Table 1. Selected Bulk Rock Compositions[a]

	Stage 2 - SV1/2	Stage 3 - P1 (650 years B. P.)				Stage 3 - 1902		Stage 3 - 1929		
	031-22b[b]	MT36Z[b]	MT38W	MT33T	MT33S[b]	062-55[c]	062-77[c]	031-42[c]	MT34P[b]	MA64[c]
Type	St Vincent	Plinian	Plinian	Pelean	Pelean	Pelean	Pelean	Pelean	Pelean	Pelean
Unit	ASF	fallout	flow	surge	surge	surge	surge	BAF	dome	BAF
Lithology	dark scoria	pumice	pumice	pumice	lithic clast	enclave	lithic clast	lithic clast	lithic clast	enclave
SiO_2	53.00	60.75	57.99	59.83	60.97	51.10	60.50	64.20	61.11	55.20
TiO_2	0.78	0.43	0.51	0.50	0.45	0.70	0.60	0.50	0.48	0.64
Al_2O_3	19.00	17.48	17.86	17.78	17.47	19.50	17.70	15.90	17.74	18.55
Fe_2O_3	8.85[d]	2.11	2.86	2.43	1.97	5.89	3.79	3.72	3.10	8.81[d]
FeO	–	4.04	4.47	4.47	4.19	3.61	2.89	2.32	3.26	–
MnO	0.17	0.17	0.22	0.19	0.18	0.20	0.17	0.19	0.18	0.21
MgO	4.24	2.17	2.41	2.64	2.20	5.30	2.80	2.00	2.29	3.88
CaO	9.60	6.16	7.05	6.46	6.15	9.50	6.20	5.40	6.24	8.37
Na_2O	2.79	3.45	3.21	3.40	3.53	3.10	3.30	4.20	3.53	2.90
K_2O	0.67	0.97	0.74	0.90	1.03	0.60	1.10	1.30	1.05	0.72
LOI	0.57	1.68	2.15	1.40	0.77	0.71	nd	0.98	0.37	0.16
P_2O_5	0.11	nd	nd	nd	nd	0.10	nd	nd	nd	0.10
Total	99.78	99.41	99.47	100.00	98.91	100.31	nd	100.71	99.35	99.54

[a] ASF, ash-and-scoria flows; BAF, block-and-ash flows; LOI, loss on ignition; nd, not determined.
[b] Sample used in the experimental studies.
[c] From *Gourgaud et al.* [1989].
[d] Total Fe as Fe_2O_3.

performed on all major oxides except MnO and H_2O [*Albarède*, 1995] to check the bulk composition of each charge, to compute the proportions of phases, and to evaluate the importance of Fe loss and quench crystallization.

[14] H_2O concentration was measured in six experimental glasses by Karl-Fischer titration using equipment and procedures identical to those described by *Behrens et al.* [1996]. Near-liquidus charges with bubble-free glasses were selected for analysis. Measured water contents were corrected for the presence of crystals, as determined from the mass balance calculations. Reproducibility was measured from repeated analyses of a standard glass of comparable weight (5–15 mg) and water concentration (6.75 wt % H_2O) as the analyzed glass samples. It is better than ±0.10 wt % H_2O (i.e., better than 2% relative for a glass with 8 wt % H_2O). Two glasses out of the six selected for Karl-Fischer titration (HAB17 and HAB18, Table 7) were analyzed by FTIR. Spectra were taken on doubly polished glass plates using a Nicolet 760 Magna FTIR instrument with attached optical microscope and equiped with a liquid N_2 cooled MCT/A detector (mercury cadmium telluride, or HgCdTe detector). Resolution was set to 2 cm^{-1}. A W source and a CaF_2 beam splitter were employed in the near-IR region (4000–8000 cm^{-1}), and a Globar source and a KBr beam splitter in the IR region (1000–4000 cm^{-1}). Spectra were accumulated for 500 scans in the near-IR region and for 50 scans in the IR region. Between 5 to 10 areas (~100 μm in diameter) were analyzed on each sample and the results averaged. Concentrations of OH, H_2O, and CO_3^{--} (sample HAB18) were determined from the peak heights of the 4500, 5200, and 1515 and 1430 cm^{-1} absorption bands using absorption coefficients from *Dixon et al.* [1995]. Glass densities were estimated from liquid densities, calculated after *Ochs and Lange* [1999]. Because of difficulties in measuring sample thickness due to the small size of experimental fragments and of uncertainties on absorption coefficients and glass densities, the accuracy of our FTIR analyses is estimated to be ±10% for H_2O (total) and ±15% for CO_3^{--}. For glasses in H_2O-undersaturated, crystal-rich charges the H_2O concentration was estimated using a modification of the "by-difference" technique [*Devine et al.*, 1995; *Martel et al.*, 1999; *Scaillet and Evans*, 1999; *Gaillard et al.*, 2001]. The difference to 100% of electron microprobe analyses was calibrated against the dissolved glass H_2O content by using the basaltic andesite starting glass and glasses analyzed by Karl-Fischer titration as secondary standards. The uncertainty on the glass H_2O content estimated with this method is ±0.5 wt %.

4. Results

4.1. Bulk Rock and Modal Compositions

[15] Previous studies on Mount Pelée [*Bourdier et al.*, 1985; *Fichaut et al.*, 1989a; *Gourgaud et al.*, 1989; *Smith and Roobol*, 1990] have stressed the wide range of major element chemistries of erupted products, from basalts (i.e., SiO_2 < 53 wt %) to dacites (i.e., SiO_2 > 62 wt %) and the lack of compositional gaps. During the recent period (stage 3), eruption products have SiO_2 between 58 and 65 wt % (~62 wt % on average, Figure 2) and include andesitic (i.e., 56 < SiO_2 < 62 wt %) and dacitic compositions, subsequently grouped for convenience under the term andesite. The new bulk rock analyses (Table 1) lie in the low-SiO_2 end of this range. No mafic magma erupted as a lava during the recent period, but mafic enclaves are present in some 1902 and 1929 products, occurring as ovoidal or spherical enclaves (up to 20 cm in diameter), as mafic droplets (up to 1 cm) in andesites, or as dark components of banded rocks [*Gourgaud et al.*, 1989]. Compositions of mafic enclaves from stage 3 (Table 1 and Figure 2) range from basalts to andesites and overlap with compositions of mafic lavas erupted during stage 2 (Figure 2). Dacites are relatively common among recent products but compositions with SiO_2 > 64 wt % (Table 1) are represented in only a few eruptive cycles, being unknown, for example, in P1 and 1902 products. Although cyclic variations of lava composition have been recognized in the recent period, erupted products since 2000 years B.P. have nearly constant average SiO_2 contents [*Fichaut et al.*, 1989a; *Smith and Roobol*, 1990]. The Mount Pelée andesites are characterized by low to medium K_2O and relatively high FeO_t/MgO (Table 1) [*Fichaut et al.*, 1989a; *Gourgaud et al.*, 1989; *Smith and Roobol*, 1990]. These compositional features are common to most active volcanoes along the Lesser Antilles arc [e.g., *Smith and Roobol*, 1990].

[16] The seven lithological units studied all have the same phenocryst assemblage, dominated (in decreasing order of abundance) by plagioclase (Plag), orthopyroxene (Opx), magnetite (Mt), and clinopyroxene (Cpx). Modal proportions of Opx markedly exceed that of Cpx. Ilmenite (Ilm) is present as trace amounts and in only a few samples. Amphibole (Amph) occurs in negligibly low modal proportions in the Mount Pelée andesites (a few crystals

per thin section). Most amphibole crystals show reaction to a Plag + Opx + Mt assemblage [see also *Gourgaud et al.*, 1989; *Smith and Roobol*, 1990]. Reaction rims up to several 100 μm thick are commonly encountered, with sizes up to 50 μm for Plag or Opx product phases. However, amphibole without any reaction rim can be found, both in Plinian and Pelean samples. The two types of amphibole may coexist in the same thin section. Olivine (Ol), present in negligible amounts in the andesites, appears as a relict phase with reaction aureoles to Plag + Opx + Mt.

[17] Total phenocryst contents of recent andesites range between 35 and 58% in volume (see also *Gourgaud et al.* [1989] for 1902 and 1929). The dome rocks have the highest values (>50%), a consequence of the presence of Plag microphenocrysts with sizes >100 μm (i.e., counted as phenocrysts). The andesites contain 29–49% Plag, 4–9% Opx, 1–2% Fe-Ti oxides, and <1% Cpx, Amph, and Ol. No systematic variation in total phenocryst content with eruption, with stratigraphic position within a given eruption or with bulk rock SiO_2 content has been documented for the recent period, and no crystalline aggregates have been identified in recent andesites [e.g., *Nakada et al.*, 1994].

[18] Mafic enclaves generally contain a higher proportion of phenocrysts than the andesites [*Gourgaud et al.*, 1989]. The typical phenocryst assemblage of the enclaves consists of olivine, clinopyroxene, orthopyroxene, plagioclase, amphibole, and magnetite. Proportions of olivine and amphibole are anticorrelated. Some enclaves are characterized by a subdoleritic texture with abundant acicular amphibole present.

4.2. Phenocrysts

[19] Electron microprobe compositions of Mount Pelée phenocrysts have been given previously by *Bourdier et al.* [1985], *Fichaut et al.* [1989b], *Gourgaud et al.* [1989], and *Smith and Roobol* [1990]. In this paper, new data are provided for the P1 eruption. Phenocrysts from the 1902 and 1929 eruption products have been reanalyzed for internal consistency with the P1 data and for comparison with the previous data set [*Gourgaud et al.*, 1989]. In addition, new electron microprobe analyses of phenocrysts from the basaltic andesite starting product are also given in Tables 2–5 to provide representative phenocryst compositions for mafic lavas from stage 2 and to allow comparison with phenocrysts from stage 3.

[20] Two main types of plagioclase phenocrysts are present in recent andesitic products: (1) simple plagioclases without anorthitic cores and (2) complex plagioclases containing anorthitic cores. The first are mostly subhedral, show well-developed oscillatory zoning, and are typically poor in vitreous inclusions. The second are mainly euhedral, and a zone of oscillatory zoning is developed only at their rims; the core may be either optically homogeneous or show complex patchy zoning; sieve-textured zones may be present. Each plagioclase population is present in proportions of approximately 80 (simple):20 (complex) and in all recent eruptions studied. Electron microprobe profiles representative of the two types of plagioclase phenocrysts are shown on Figure 3. Note the homogeneity of composition of the anorthitic core (Figure 3b), the amplitude (10–15% An) of the chemical oscillations (Figure 3c) and the marked compositional change at the core-rim boundary (Figure 3b). Plagioclase phenocrysts in recent Mount Pelée products have a wide range of compositions, from An_{50} to An_{90}. However, two groups of compositions emerge from electron microprobe profiles (Figure 3) and histograms of plagioclase An content [*Gourgaud et al.*, 1989]. The first group corresponds to anorthitic cores which have a well-defined range of compositions between An_{85} and An_{90} on average, with values up to An_{94}, and the second group to the phenocryst rims (range An_{50-65}). Compositions representative of these two groups are given in Table 2. Plagioclases analyzed in 2 amphibole reaction rims are An_{86} and An_{87}, identical to a plagioclase inclusion in another amphibole (An_{86}). A plagioclase from an olivine (Fo_{62}) reaction rim is An_{80} (Table 2). Only minor differences between plagioclases textures and chemistries can be detected between eruptions: plagioclase rims in the 1929 products have An_{50-55} compositions; in the P1 samples the range of composition of the plagioclase rims is An_{55-60} (and identical in the Pelean and Plinian units, Table 2), and in the 8 May 1902 surge, plagioclase rim compositions are inbetween those in 1929 and P1. The mafic enclaves from the 1902 and 1929 products have in common with the andesites the presence of a maximum frequency at An_{85-90}. A second maximum frequency (An_{70-75}) corresponds to plagioclase rims [*Gourgaud et al.*, 1989].

[21] Orthopyroxene phenocrysts in recent andesites are either homogeneous or slightly normally zoned, with core-to-rim variations <6% En. In all studied samples except the 1929 dome, orthopyroxenes cover a narrow range of compositions between En_{52} and En_{60}, with Wo contents mostly $\leq$3% and Al_2O_3 contents mostly <1 wt %. In the 1929 dome, Opx are commonly surrounded by a dark red oxydation rim, and their compositions extend to En_{69}, i.e., more Mg-rich than in other samples (Figure 4). These magnesian orthopyroxenes are interpreted as partially reequilibrated during eruption. Representative compositions of orthopyroxene phenocrysts in recent andesites and the 1929 dome are given in Table 3. There is not a systematic difference in orthopyroxene composition between the Pelean and Plinian units of P1 or between the different eruptions studied (apart from the reequilibrated compositions in the 1929 dome). Orthopyroxenes in olivine reaction rims have compositions (En_{56-61}) in the range of the most magnesian phenocrysts. In the mafic enclaves they are on average slightly more magnesian than phenocrysts in andesites, extending up to En_{65} (Figure 4 and Table 3). Olivines show the same behavior: They have Fo between 65 and 77 in the mafic enclaves [*Gourgaud et al.*, 1989], while more Fe-rich compositions (up to Fo_{62}) are found in the andesites (Table 3). Clinopyroxenes are all augites with a limited compositional range: $En_{37-44}Wo_{39-43}Fs_{16-22}$ (Table 3). There is no clear variation with lithological type and augites from the mafic enclaves plot together with phenocrysts from the andesites (Figure 4). Al_2O_3 contents range between 1 and 2 wt %, with average Al(IV) and Al(VI) values of ~0.05 and 0.02, respectively (6 O basis). One analysis out of 23 is Al_2O_3-rich and SiO_2-poor (Table 3), yielding an Al(IV) value of 0.16. Proportions of Fe^{3+} (i.e., 100 $Fe^{3+}/(Fe^{3+} + Fe^{2+})$, with Fe^{3+} calculated after *Papike et al.* [1974]) are 10% on average (with no difference between the andesites and the mafic enclaves) and reach 24% for the Al_2O_3-rich augite. Pyroxene thermometry (1 bar values [*Lindsley*, 1983]) yields quite a large range of temperatures. Values of 725–975°C and 720–1070°C are obtained from orthopyroxene and augite compositions, respectively. For orthopyroxenes, most phenocryst compositions in andesites yield temperatures near 850°C. The mafic enclaves reach values up to 925–975°C. For clinopyroxenes the average temperature is 870°C with no difference between andesites and mafic enclaves.

[22] Magnetites from the P1 fallout and surge, 1902 products, and 1929 BAF are optically and chemically homogeneous. In contrast, magnetites from the 1929 dome systematically contain ilmenite lamellae and are not considered further. Most magnetite phenocrysts in andesites range between Mt_{67} and Mt_{71} (Table 4 and Figure 5) using the projection scheme of *Andersen et al.* [1993]. They are characterized by TiO_2 and Al_2O_3 of 10–11.5 and 2–3 wt %, respectively. Magnetites from the mafic enclaves have the same range of Mt contents as magnetite phenocrysts in andesites (Figure 5), although the former tend to be slightly more Al-rich and magnesian than the latter. No systematic variation of magnetite composition can be detected between the studied eruptions and between the Plinian and Pelean units of P1. However, a few phenocrysts have compositions outside the normal range, with Mt contents of ~74, TiO_2 < 9 wt %, and Al_2O_3 > 3 wt % (Figure 5 and Table 4). Magnetites from amphibole reaction rims and magnetite inclusions in amphibole (Table 4) and olivine [*Gourgaud et al.*, 1989] also have elevated Mt contents (>75), low TiO_2 (down

Table 2. Selected Compositions of Plagioclase[a]

	Stage 2 - SV1/2 ASF	Stage 3 - P1									Stage 3 - 1902			Stage 3 - 1929					
		Fallout			Surge						Dome	Enclave		Dome			BAF		Enclave
	Core	Rim	Interm.	Core	Rim	Interm.	Interm.	Reaction[b]	Reaction[c]	Inclusion[d]	Rim[e]	Core[e]	Rim[e]	Rim	Interm.	Core	Rim	Interm.	Core[e]
SiO_2	48.0	53.7	52.0	45.8	54.6	51.0	53.2	47.0	46.6	46.3	55.7	46.4	51.6	54.8	48.6	46.0	54.8	53.4	46.8
TiO_2	0.00	0.08	0.05	0.02	0.03	0.08	0.00	0.00	nd	nd	nd	nd	nd	0.03	0.07	0.06	0.04	0.03	nd
Al_2O_3	33.2	29.1	30.9	34.6	28.7	31.4	29.8	32.7	33.8	34.2	27.8	33.5	30.3	28.5	32.2	35.1	28.4	29.3	33.2
FeO	0.50	0.34	0.52	0.51	0.44	0.43	0.48	0.98	0.52	0.50	0.01	0.49	0.56	0.32	0.76	0.52	0.52	0.53	0.50
MnO	0.00	0.00	0.00	0.04	0.03	0.22	0.00	0.03	0.07	0.00	nd	nd	nd	0.09	0.15	0.00	0.12	0.00	nd
MgO	0.08	0.04	0.02	0.09	0.03	0.03	0.05	0.06	0.05	0.06	nd	nd	nd	0.00	0.09	0.07	0.00	0.06	nd
CaO	16.5	12.0	13.5	18.0	10.8	13.2	12.4	16.4	17.8	15.6	10.8	17.5	13.2	10.6	16.2	18.8	10.7	12.3	17.2
Na_2O	1.95	4.62	3.79	1.08	4.73	3.29	4.31	2.32	1.49	1.37	5.44	1.46	3.69	5.26	2.58	1.08	5.31	4.48	1.68
K_2O	0.05	0.04	0.05	0.00	0.17	0.10	0.08	0.04	0.02	0.03	0.30	0.00	0.04	0.17	0.00	0.03	0.12	0.02	0.03
Total	100.3	99.9	100.8	100.1	99.5	99.8	100.3	99.5	100.4	98.1	100.1	99.4	99.4	99.8	100.7	101.7	100.0	100.1	99.4
Ab	17.5	41.0	33.6	9.8	43.7	30.9	38.3	20.3	13.1	13.7	46.9	13.2	33.6	47.0	22.3	9.4	47.1	39.8	15.0
An	82.2	58.8	66.1	90.2	55.3	68.5	61.1	79.5	86.7	84.8	51.4	86.8	66.2	52.0	77.7	90.5	52.2	60.1	84.8
Or	0.3	0.2	0.3	0.0	1.0	0.6	0.6	0.2	0.2	0.2	1.7	0.0	0.02	1.0	0.0	0.0	0.7	0.1	0.2

[a] ASF, ash-and-scoria flows; BAF, block-and-ash flows; interim., intermediate; nd, not determined.
[b] From olivine reaction rim.
[c] From amphibole reaction rim.
[d] Inclusion in amphibole.
[e] From *Gourgaud et al.* [1989].

Table 3. Selected Compositions of Pyroxene and Olivine[a]

	Stage 2 - SV1/2 ASF			Stage 3 - P1									Stage 3 - 1902					Stage 3 - 1929							
				Fallout				Surge					Dome		Enclave			Dome				BAF		Enclave	
	Opx(r)	Cpx(c)	Ol(r)	Opx(c)	Opx(r)	Opx	Cpx	Opx	Opx	Cpx	Opx[b]	Ol[c]	Opx[d]	Cpx[d]	Opx[d]	Cpx[d]	Ol[d]	Opx	Opx	Cpx	Cpx	Opx	Cpx	Opx[d]	Cpx[d]
SiO_2	53.9	46.0	39.7	52.3	51.7	52.0	51.5	52.9	53.1	52.0	52.4	37.1	52.4	51.8	53.1	51.8	39.1	52.9	54.2	52.0	48.8	51.5	51.5	52.1	52.4
TiO_2	0.20	1.41	0.04	0.05	0.12	0.10	0.23	0.13	0.06	0.29	0.15	0.03	0.14	0.32	0.10	0.39	0.00	0.20	0.10	0.51	0.60	0.16	0.36	0.17	0.22
Al_2O_3	1.46	10.0	0.00	0.49	0.86	0.59	0.99	0.78	0.53	1.74	0.78	0.01	0.59	1.61	0.84	2.47	0.00	1.68	0.87	2.36	4.42	0.68	1.62	0.98	1.06
FeO	18.0	6.79	18.2	24.8	27.2	23.5	11.9	22.8	25.4	11.9	25.3	33.2	25.1	11.5	20.6	12.1	21.9	21.2	19.1	10.4	10.6	24.4	12.7	24.8	11.4
MnO	0.34	0.00	0.10	1.12	1.10	1.07	0.82	0.96	1.13	0.37	1.13	0.90	1.18	0.60	1.08	0.93	0.43	0.76	0.61	0.36	0.38	1.00	0.60	1.10	0.59
MgO	24.6	12.5	42.2	20.0	18.7	20.5	13.4	21.5	19.3	12.9	19.3	30.9	18.7	12.8	22.8	13.4	38.8	22.2	23.5	14.3	14.1	19.8	13.6	19.3	13.0
CaO	1.51	22.5	0.11	1.35	1.05	1.25	20.3	1.48	1.3	19.1	1.27	0.04	1.26	19.9	1.43	19.5	0.05	1.61	1.87	20.9	21.0	1.50	19.4	1.20	20.7
Na_2O	0.01	0.22	0.00	0.15	0.00	0.06	0.32	0.06	0.02	0.31	0.00	0.03	0.05	0.39	0.02	0.19	0.00	0.03	0.00	0.26	0.00	0.07	0.24	0.06	0.32
K_2O	0.00	0.00	0.00	0.02	0.00	0.00	0.00	0.01	0.01	0.01	0.00	0.00	0.00	0.00	0.00	0.00	0.00	0.00	0.00	0.00	0.00	0.00	0.00	0.00	0.00
Total	100.0	99.4	100.4	100.3	100.7	99.1	99.5	100.6	100.9	98.6	100.3	102.2	99.4	98.9	100.0	100.8	100.3	100.6	100.3	101.1	99.9	99.1	100.0	99.7	99.7
$100.X_{Mg}$	68.8	38.7	80.5	56.2	52.9	58.3	38.2	59.9	55.0	38.4	55.6	62.3	54.4	37.9	63.3	38.7	75.5	62.2	65.5	40.4	39.9	56.4	38.9	55.7	37.5
$100.X_{Ca}$	3.0	49.7	0.0	2.7	2.1	2.5	41.6	3.0	2.6	41.1	2.6	0.0	2.6	42.1	2.9	40.3	0.0	3.2	3.7	42.6	42.7	3.1	39.8	2.5	43.0
$100.X_{Fe}$	28.2	11.6	19.5	41.1	45.0	39.2	20.2	37.1	42.4	20.5	41.8	37.6	43.0	20.0	33.8	21.0	24.5	34.6	30.8	17.0	17.4	40.5	21.3	41.8	19.5

[a] ASF, ash-and-scoria flows; BAF, block-and-ash flows; nd, not determined; c, core; r, rim. X_{Mg} = Mg / (Mg+Ca+Fe); X_{Ca} = Ca / (Mg+Ca+Fe); X_{Fe} = Fe / (Mg+Ca+Fe) with total Fe as FeO.
[b] From olivine reaction rim.
[c] With Plag (Table 2) and Opx reaction rim.
[d] From *Gourgaud et al* [1989].

Table 4. Selected Compositions of Fe-Ti Oxide[a]

	Stage 2 - SV1/2 ASF	Stage 3 - P1									Stage 3 - 1902		Stage 3 - 1929						
		Fallout				Surge					Dome	Enclave	BAF						Enclave
	Mt	Mt	Mt[b]	Mt	Mt	Mt	Mt	Mt	Mt[b]	Mt[c]	Mt[d]	Mt[d]	Mt	Mt	Mt[e]	Mt[e]	Ilm[e]	Ilm[e]	Ilm[e]	Mt[d]
SiO_2	0.20	0.13	0.13	0.24	0.04	0.15	0.03	0.21	0.10	0.12	0.12	0.15	0.12	0.33	0.10	0.11	0.08	0.35	0.00	0.02
TiO_2	8.46	11.4	7.96	10.4	10.6	11.0	10.1	8.56	8.33	4.32	11.3	11.3	10.1	8.70	10.3	10.5	46.1	45.4	46.3	10.6
Al_2O_3	4.44	2.09	3.53	2.40	2.03	2.27	2.29	3.46	3.43	6.04	1.19	2.71	2.56	3.42	2.46	2.12	0.23	0.21	0.07	2.33
FeO	78.1	79.7	81.4	81.9	79.6	79.8	80.1	80.8	81.2	80.5	82.4	80.0	80.6	78.7	80.6	79.7	50.7	50.9	51.1	81.6
MnO	0.32	0.70	0.36	0.48	0.48	0.51	0.61	0.25	0.50	0.54	0.83	0.53	0.62	0.42	0.53	0.40	1.06	0.73	0.85	0.63
MgO	2.96	1.20	1.51	1.20	1.15	1.22	1.24	1.47	1.65	1.74	0.17	1.60	0.79	0.96	0.86	0.84	1.70	1.86	1.91	1.11
Total	94.5	95.2	94.9	96.6	93.9	95.0	94.4	94.8	95.2	93.3	96.0	96.3	94.8	92.5	94.9	93.7	99.9	99.5	100.2	96.3
Mt	74.2	67.2	76.4	70.1	68.9	68.0	70.5	74.4	75.6	86.9	68.1	67.3	70.5	73.4	69.7	68.8	–	–	–	69.7
Hm	–	–	–	–	–	–	–	–	–	–	–	–	–	–	–	–	15.1	16.0	15.6	–

[a] ASF, ash-and-scoria flows; BAF, block-and-ash flows.
[b] From amphibole reaction rim.
[c] Inclusion in amphibole.
[d] From *Gourgaud et al.*, [1989].
[e] Coexisting in the same thin section.

Table 5. Selected Compositions of Amphibole[a]

	Stage 2 -SV1/2 ASF		Stage 3 - P1								Stage 3 - 1902			Stage 3 - 1929			
			Fallout						Surge		Surge		Enclave	Dome		BAF	Enclave
	Unrim.	Unrim.	Unrim.	Unrim.	Rim	Rim	Rim(c)	Rim(r)	Unrim.	Unrim.	Unspec.[b]	Unspec.[b]	Unspec.[b]	Unspec.[b]	Unspec.[b,c]	Unspec.[b]	Unspec.[b]
SiO_2	40.6	42.2	44.4	41.9	43.6	41.9	42.6	45.1	44.6	43.9	42.4	46.5	42.7	42.8	47.7	45.1	42.5
TiO_2	1.84	1.93	1.53	1.57	1.52	1.43	1.49	1.47	1.49	1.55	1.54	1.54	1.61	1.87	1.29	1.85	1.84
Al_2O_3	16.0	13.3	11.9	14.2	12.9	14.3	13.7	11.7	12.4	13.0	13.4	8.3	12.9	12.7	6.82	8.09	13.5
FeO	8.74	11.6	11.5	13.2	12.1	13.2	12.3	12.6	12.4	11.8	12.4	15.4	13.3	11.9	17.4	16.1	11.3
MnO	0.18	0.07	0.20	0.16	0.10	0.13	0.16	0.34	0.22	0.05	0.33	0.43	0.26	0.12	0.59	0.42	0.19
MgO	15.0	14.2	15.2	13.3	14.8	12.6	14.4	14.7	14.6	14.7	13.9	13.6	13.2	14.3	12.9	13.3	14.3
CaO	12.3	11.5	10.7	10.5	10.4	10.7	10.5	10.3	10.5	10.9	11.3	10.4	10.9	11.0	10.5	10.7	11.12
Na_2O	2.50	2.26	2.14	2.36	2.38	2.32	2.26	2.13	2.20	2.31	2.28	1.61	2.12	2.29	1.19	1.45	2.30
K_2O	0.43	0.34	0.16	0.17	0.13	0.17	0.14	0.11	0.14	0.20	0.21	0.17	0.13	0.27	0.06	0.24	0.18
Total	97.6	97.4	97.7	97.4	97.9	96.8	97.6	98.5	98.6	98.4	97.8	98.0	97.3	97.3	98.5	97.2	97.2

[a] ASF, ash-and-scoria flows; BAF, block-and-ash flows; unrim., amphibole without a reaction rim; rim, amphibole with a reaction rim; unspec., amphibole texture not specified ; c, core ; r, rim.
[b] From *Gourgaud et al.* [1989].
[c] Amphibole in a dioritic cumulate block.

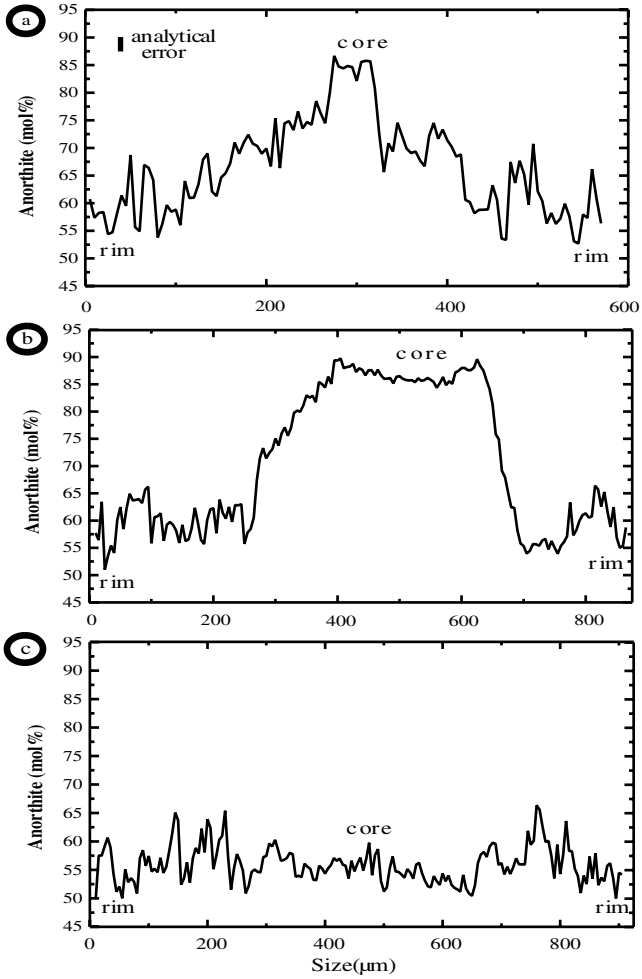

Figure 3. Representative electron microprobe profiles of plagioclase phenocrysts from recent eruption products of Mount Pelée: (a) plagioclase with calcic core, P1 surge; (b) plagioclase with calcic core, May 8, 1902 surge; and (c) plagioclase without calcic core, 1929 dome.

to 4 wt %), and high Al_2O_3 (up to 6–8 wt %). Ilmenite was found (two crystals) in only one thin section of 1929 BAF, yielding compositions in the range Hm_{12-18} (Table 4). $T - \log f_{O2}$ calculations were performed from the average compositions of these two ilmenites and of two touching magnetites (four Fe-Ti oxide pairs in total). The formulation of *Ghiorso and Sack* [1991] was preferred, as justified by *Martel et al.* [1998]. Results yield temperatures of 875, 854, 848, and 880°C, and ΔNNO values (= $\log f_{O2} - \log f_{O2}$ of the NNO buffer at 2 kbar) of +0.5, +0.3, +0.4, and +0.5, respectively. *Gourgaud et al.* [1989] report ilmenite compositions for a sample of the 8 May 1902 surge and a mafic enclave in a 1929 BAF. These two Fe-Ti oxide pairs yield temperatures of 840 and 902°C and ΔNNO of +0.4 and +0.8, respectively, when recalculated following *Ghiorso and Sack* [1991].

[23] Amphiboles show important compositional variations. SiO_2 and Al_2O_3 contents range from 41 to 48 and 16 to 7 wt %, respectively (Table 5). There is a well-marked positive correlation between Al(IV) and the number of cations in site A calculated on a 23 O basis. However, the variation is discontinuous and a compositional gap exists between Al(IV) = 1.5 and 1.25 (Figure 6), corresponding to Al_2O_3 contents between ~11 and ~8 wt %, respectively. Most amphiboles in recent Mount Pelée products are pargasitic hornblendes, with Al(IV) ≥ 1.5, number of cations in site A > 0.6 per formula unit (pfu) and Mg # (calculated with total Fe as FeO) between 0.62 and 0.70 (Figure 6). These pargasitic hornblendes are found in all recent eruption products, either Pelean or Plinian, and in andesites as well as in mafic enclaves. Pargasitic hornblendes with and without a Plag + Opx + Mt reaction rim are not compositionally different from each other (Table 5) and are plotted together on Figure 6. Another population of amphiboles (edenitic hornblendes) is restricted to rare evolved compositions (bulk rock SiO_2 > 63 wt %) and a few dioritic cumulate blocks in the 1929 dome [*Fichaut et al.*, 1989b; *Gourgaud et al.*, 1989]. They make up a very small proportion of amphiboles present. These edenitic hornblendes have Al(IV) ≤ 1.3, the number of cations in the site A < 0.6 pfu and Mg # between 0.55 and 0.62 (Figure 6).

4.3. Glasses

[24] Electron microprobe analyses of Mount Pelée glasses have been given previously by *Bourdier et al.* [1985] and *Fichaut et al.* [1989a, 1989b] for mafic lavas and cumulates (both gabbroic and dioritic), mainly from stage 2. For stage 3, textural descriptions of glass inclusions and matrix glasses and H_2O concentration data have been given by *Martel et al.* [1998, 2000]. Here we detail glass major element compositions in recent eruption products.

[25] All glass inclusions are rhyolitic (total range of 74–81 wt % SiO_2). No systematic correlation exists with the nature (or composition) of the host crystal (Table 6). Most inclusions from the 1902 and 1929 Pelean products are characterized by high to very high SiO_2 and K_2O (up to 81 and 5%, respectively) and low Al_2O_3 and CaO (as low as 8 and 0.5%, respectively) and reflect important postentrapment modifications [*Martel et al.*, 2000]. Matrix glasses (P1, microlite-free or microlite-poor pumice lumps from the Plinian units, microlite-poor lithics, and dense pumices from the Pelean surge; 1929, BAF lithics) are also all rhyolitic (74.0–76.5 wt % SiO_2, Table 6). Compositions of matrix glasses from the Plinian and Pelean samples from P1 are grouped near 75 wt % SiO_2 on average and are almost identical to the P1 glass inclusions (Table 6). Matrix glasses from the 1929 BAF extend up to 80 wt % SiO_2, a result of the high crystallinity of the groundmass in these samples. Interstitial glass in a dioritic cumulate from 1902 [*Fichaut et al.*, 1989b] is identical in composition to glass inclusions and matrix glasses from P1, 1902, and 1929. Therefore all glasses from recent eruption products have rhyolitic compositions, although it should be mentioned that there are presently no data for glasses in mafic enclaves. More mafic glasses (basaltic to dacitic) are known at Mount Pelée, but their occurrence is restricted to stage 2 products (interstitial glasses in gabbroic cumulates and residual glasses in mafic lavas [*Bourdier et al.*, 1985; *Fichaut et al.*, 1989a, 1989b], see below).

[26] Nearly all the H_2O concentration data for glass inclusions of the recent period have been obtained with the by-difference method (Table 6, uncertainty of ±0.5 wt %). *Martel et al.* [1998, 2000] reported the analysis of one glass inclusion by FTIR. H_2O concentrations range between 4.3 and 7.1 wt % H_2O in the P1 Plinian fallout (number of inclusions analyzed, n = 14) and between 3.0 and 7.8 wt % H_2O in the pumice flow (n = 10). In the P1 surge, glass inclusions have H_2O contents of 0.4–7.1 wt % and 2.2–6.9 wt % in the lithics (n = 14) and dense pumices (n = 28), respectively. For comparison, melt H_2O contents calculated from the plagioclase-melt model of *Housh and Luhr* [1991] yield values ranging between 1.9 and 5.5 wt % H_2O for the P1 samples, i.e., within the analytically determined range (see *Martel et al.* [1998] for the details of the calculations). Inclusions from the 8 May 1902 (n = 5), 1929 dome (n = 10), and BAF (n = 18) contain low amounts of H_2O (0.9–2.5, <2.6, and <2.0 wt % H_2O, respectively, see Table 6).

4.4. Experimental Results

[27] Details about experimental conditions and results are given in Table 7. Nineteen near-liquidus experiments are available for the

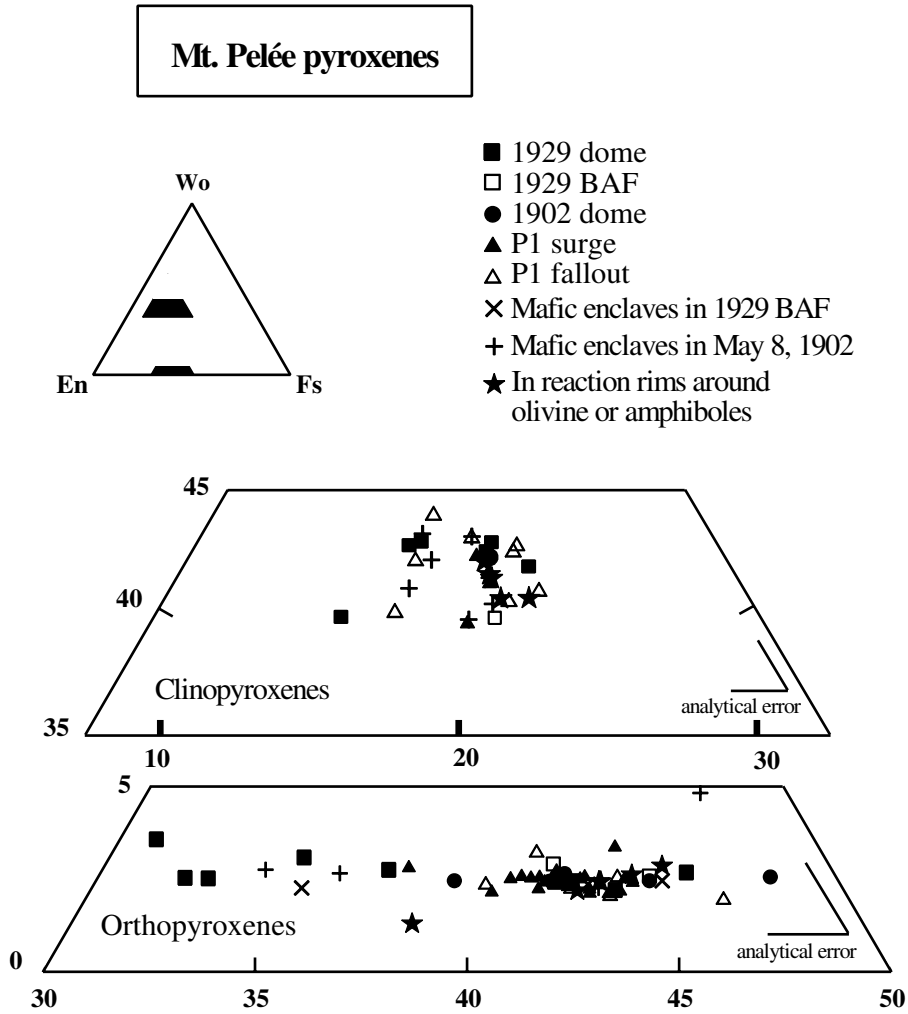

Figure 4. Compositions of pyroxene phenocrysts from recent eruptions products of Mount Pelée. Data for the 1902 dome and mafic enclaves are from *Gourgaud et al.* [1989].

basaltic andesite composition at 4 kbar. One additional experiment (P1D, Table 7) has been performed on an andesite sample to extend the 4 kbar database for this composition [*Martel et al.*, 1999]. The basaltic andesite experiments cover a substantial range of melt H_2O concentrations (from 8.3 to 2.6 wt %, Table 7) and crystal contents (from 0 to 61% by weight, Table 7). They can be divided into three groups, depending on f_{O2}: $\Delta NNO < +1$, $+1 < \Delta NNO < +1.5$, and $\Delta NNO > +2.5$.

[28] The Karl-Fischer titration data yielded 8.2 ± 0.12 wt % H_2O on average for the four H_2O-saturated glasses HAB6, HAB17, HAB20, and HAB23 (Table 7) and 8.2 wt % has been taken as the H_2O concentration of the two other H_2O-saturated glasses (HAB1, HAB11) that could not be analyzed because of the abundance of crystals (Table 7). For comparison, the H_2O solubility calculated for the basaltic andesite is 8.5 wt % at 4 kbar, 1025°C [*Burnham*, 1979]. For glass HAB17 the Karl-Fischer and FTIR data are in agreement within error. However, for glass HAB18 the FTIR is significantly above the Karl-Fischer concentration (6.7 versus 5.4 wt % H_2O, Table 7). The Karl-Fischer value is preferred here because it is the most consistent with the CO_2 concentration measured in that glass (1120 ± 190 ppm): C-O-H fluid composition and speciation [e.g., *Scaillet et al.*, 1995] calculated for charge HAB18 at known P, T, f_{H2}, and f_{H2O} (computed from the Karl-Fischer H_2O concentration, Table 7) yields a f_{CO2} and a concentration of dissolved CO_2 [*Holloway and Blank*, 1994] of ~850 ppm, near the lower limit of the concentration measured in the glass; similar calculations with f_{H2O} computed from the IR H_2O concentration yield 440 ppm of dissolved CO_2, more than twice as less than measured. The presence of dissolved CO_2 in the H_2O-undersaturated glasses introduces an additional source of error for the estimation of H_2O by difference. However, C-O-H fluid calculations show that concentrations of dissolved CO_2 are <2000 ppm (i.e., 2030 ppm in the charge with the lowest aH_2O, HAB25), i.e., are much less than the uncertainty of the by-difference method (±0.5 wt % H_2O).

[29] All experiments reported in Table 7 are crystallization experiments where crystals have nucleated and grown from the melt. Phase appearance sequences and mineral compositional variations have not been reversed, and therefore equilibrium cannot be rigorously demonstrated. Two reconnaissance melting experiments were performed by using the basaltic andesite powder (ground to <50 μm) as starting material, instead of glass. These experiments yielded disequilibrium phase assemblages characterized by the presence of incompletely reacted, relictual plagioclases. Marked compositional zonations were found in both glass and plagioclase, despite the elevated temperatures (1041°C), long run durations (53 hours) and high meltwater contents (initial $H_2O/(H_2O + CO_2) = 0.9$) of these experiments. Consequently, crystallization

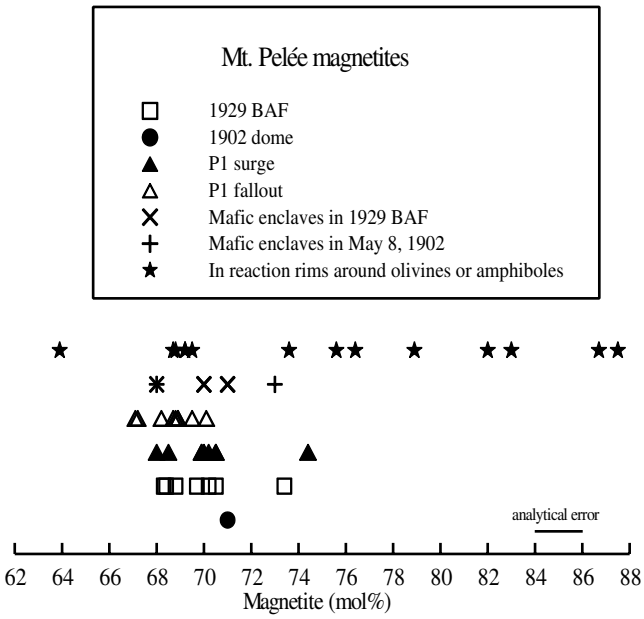

Figure 5. Compositions of magnetite from recent eruption products of Mount Pelée. Data for the 1902 dome and mafic enclaves are from *Gourgaud et al.* [1989].

experiments are preferred (see *Martel et al.* [1999] and *Scaillet and Evans* [1999] for further considerations about experimental strategy). We believe that equilibrium has been closely approached in our crystallization experiments (Table 7) for the following reasons:

1. Textural and morphological data for the experimental charges (homogeneous crystal distribution and sizes, euhedral crystal shapes) indicate easy and fast nucleation. The presence of quench crystals in some of the charges (see below) and the noted abundant quench crystallization in experiments that were not ended with the rapid-quench device (typical quench rate: 100°C mn^{-1}, experiments not reported in Table 7) provide additional evidence for fast crystallization kinetics. Although time series experiments were not performed, no large variation in crystal size was noticed between the shortest (13 hours) and the longest experiments (99 hours). The exception is charge HAB25 (one from the shortest experiment), which has a glass H_2O content much lower than all the others (2.6 wt % H_2O, Table 7) and smaller crystal sizes. This suggests that the fast crystallization kinetics observed in this study is related to the elevated experimental melt H_2O concentrations (all but three glasses have $\geq$5 wt % H_2O, Table 7).

2. Mineral phases and glasses from this study are essentially homogeneous (standard deviations in Table 8) and their compositions vary regularly and smoothly with experimental conditions. Calculated mineral-melt partition coefficients agree well with accepted values (see below), suggesting a close approach to chemical equilibrium.

3. Mass balance calculations show that a constant bulk silicate composition has been maintained. Apparent losses or gains of FeO from mass balance calculations are $\leq$1% in 14 charges, exceed 5% in only two charges and are never >6% (Table 7). The Au capsule in HAB6 has a Fe concentration below detection ($\sim$500 ppm), and the FeO concentration of HAB17 (the only charge above the liquidus) is identical within error to that of the starting glass (Table 8). This demonstrates that Fe loss to the capsules was not significant in this study.

4. Quench crystals were detected by SEM in 8 out of the 20 experimental charges (Table 7). However, calculated mineral-melt partition coefficients do not depend on the presence of quench crystals (e.g., compare the Fe-Mg exchange Kd between Cpx and liquid in charges HAB18 and HAB19, Tables 7 and 8). In the same way, sums of residuals of mass balance calculations (always <1) are not correlated with the presence of quench crystals. Overall, this demonstrates that in this study, quench crystallization did not appreciably affect the glass composition.

[30] Crystalline phases present, after being detected by SEM, were usually confirmed from their electron microprobe analysis. However, in HAB3 and HAB8, amphibole was detected by SEM, but its presence could not be confirmed after an extensive electron microprobe search. Therefore amphibole has been omitted from the phase assemblage in these two charges. Generally, analysis of the glass in charges with >60 wt % crystals proved difficult, and in two charges (HAB3 and HAB13) the absence of glass pools of sufficient size prevented glass analysis. Nevertheless, compositions of crystalline phases present in these two charges are given (Table 8).

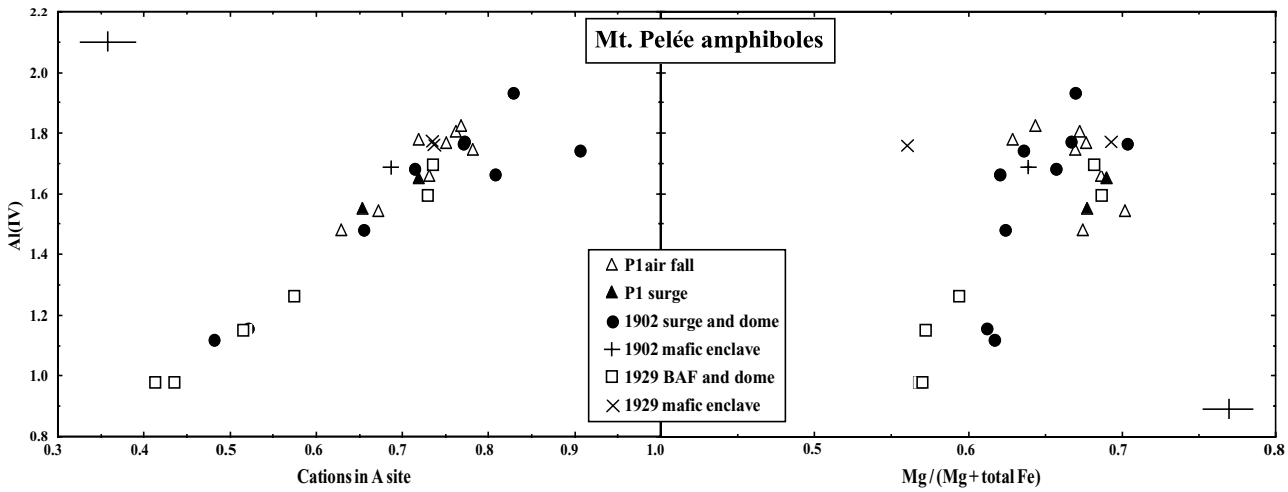

Figure 6. (left) Al(IV) versus number of cations in site A and (right) Mg/(Mg + total Fe) for amphibole phenocrysts from recent eruption products of Mount Pelée. Data for the 1902 and 1929 products are from *Gourgaud et al.* [1989]. Error bars shown as crosses (top left and bottom right). Amphibole structural formulae calculated on a 23 oxygen basis with all Fe as FeO.

Table 6. Selected Compositions of Glasses[a]

	P1[b]													1902 Surge	1929 BAF	
	Fallout							Flow		Surge						
	Inclus. (Plag)	Inclus. (Plag)	Inclus. (Plag)	Inclus. (Plag)	Inclus. (Opx)	Inclus. (Opx)	Matrix (n = 12)	Inclus. (Plag)	Matrix (n = 5)	Inclus. (Opx)	Inclus. (Plag)	Inclus. (Plag)	Matrix (n = 37)	Inclus. (Plag)	Inclus. (Plag)	Matrix (n = 4)
SiO_2	75.4	74.7	74.4	75.6	74.8	74.6	76.1 (4)	75.9	74.0 (2)	75.8	75.7	75.1	75.0 (3)	76.8	76.6	76.3 (2)
TiO_2	0.23	0.32	0.30	0.29	0.16	0.29	0.24 (17)	0.17	0.28 (6)	0.38	0.39	0.33	0.31 (2)	0.28	0.36	0.29 (8)
Al_2O_3	13.0	13.3	13.7	13.0	13.5	13.5	12.7 (6)	13.1	13.4 (2)	12.7	12.5	13.0	13.2 (1)	10.3	11.7	12.4 (3)
FeO	2.70	2.67	2.65	2.11	2.66	2.67	2.12 (9)	2.12	2.87 (20)	2.77	2.57	2.53	2.68 (10)	2.87	2.02	2.01 (44)
MnO	0.10	0.06	0.04	0.00	0.08	0.19	0.07 (4)	0.06	0.05 (4)	0.00	0.33	0.15	0.11 (2)	0.05	0.07	0.08 (10)
MgO	0.40	0.49	0.39	0.40	0.26	0.18	0.33 (4)	0.37	0.48 (4)	0.16	0.42	0.34	0.43 (2)	0.39	0.27	0.27 (2)
CaO	2.18	2.55	2.66	2.25	2.51	2.48	2.19 (8)	2.61	2.88 (10)	1.90	1.80	2.40	2.46 (8)	0.88	1.51	1.81 (6)
Na_2O	3.83	3.89	3.82	4.16	3.92	3.89	4.29 (33)	3.81	4.26 (24)	4.03	4.09	4.07	3.88 (4)	3.49	5.19	4.55 (6)
K_2O	2.13	1.98	2.11	2.12	2.12	2.22	1.96 (8)	1.83	1.79 (14)	2.24	2.20	2.05	1.99 (4)	4.95	2.24	2.30 (14)
Total	94.0	93.6	92.8	92.7	93.6	94.1	97.1 (11)	92.0	95.8 (9)	93.6	95.3	94.4	97.9 (7)	97.6	96.8	99.1 (4)
H_2O	4.8	5.5	5.9	6.0	5.2	4.7	1.6–2.3	6.8	2.8–3.8	4.8	4.0	5.5	0.0–1.8	0.9	1.7	0.0–0.0

[a] BAF, block-and-ash flows. Data normalized to 100% anhydrous. Original unnormalized total is reported. inclus., glass inclusion; matrix, matrix glass. Data for the matrix glasses are averages of multiple analyzes with standard deviations (1σ) given in parentheses in terms of the least unit cited. H_2O content using the by-difference method (see text and *Martel et al.*, [1998, 2000]). For matrix glasses the range of H_2O content is given rather than the average value.

[b] Recent period (stage 3).

Table 7. Experimental Conditions and Results[a]

Charge	$XH_2Oin.$	H_2O in Glass, wt %	aH_2O	log f_{O2}, bars	ΔNNO, bars	Results[b]	ΣR^2	Fe Loss,[c] %
				Run 1, 3988 bars, 949°C, f_{H2} = 8.1 bars, 99 hours				
HAB1	1.00	8.2[d]	1.00	−10.1	+0.8	Gl(58), Plag(16), Amph(26)	0.60	−6
HAB2	0.77	6.8[e]	0.82	−10.3	+0.6	Gl(46), Plag(23), Amph(31), Opx(<1)	0.30	1
HAB3	0.61	nd (< 6.8)	nd	< − 10.3	< + 0.6	Gl, Plag, Opx, Cpx, Mt, Ilm	nd	nd
				Run 2, 4270 bars, 1000°C, f_{H2} = 14.3 bars, 40 hours				
HAB6	1.00	8.1[f]	0.90	−9.6	+0.5	Gl(99), Cpx(1), Qu	0.17	2
HAB7	0.79	6.8[e]	0.76	−9.7	+0.4	Gl(74), Plag(13), Amph(5), Cpx(7), Ol(1), Qu	0.22	−5
HAB8	0.62	5.9[e]	0.65	−9.9	+0.2	Gl(49), Plag(33), Opx(7), Cpx(11), Qu	0.61	−1
				Run 3, 3949 bars, 1016°C, f_{H2} = 9.7 bars, 22 hours				
HAB17	1.00	8.1[f]/ 8.6[g]	0.93	−9.0	+0.8	Gl(100), Qu	0.16	3
HAB18	0.79	5.4[f]/6.7[g]	0.62	−9.4	+0.4	Gl(96), Plag(3), Cpx(1)	0.23	<1
HAB19	0.61	4.3[e]	0.50	−9.6	+0.2	Gl(69), Plag(20), Opx(3), Cpx(8), Qu	0.04	<1
				Run 4, 4002 bars, 945°C, f_{H2} = 4.6 bars, 60 hours				
HAB11	1.00	8.2[d]	0.92	−9.7	+1.3	Gl(64), Plag(11), Amph(23), Mt(2), Qu	0.39	<1
HAB12	0.76	6.9[e]	0.82	−9.8	+1.2	Gl(47), Plag(24), Amph(26), Mt(3)	0.34	<1
HAB13	0.58	nd (<6.9)	nd	< −9.8	< + 1.2	Gl, Plag, Opx, Cpx, Mt	nd	nd
				Run 5, 4048 bars, 995°C, f_{H2} = 4.3 bars, 49 hours				
HAB14	0.81	6.4[e]	0.72	−8.9	+1.3	Gl(79), Plag(10), Amph(6), Cpx(4), Mt(1), Qu	0.07	<1
HAB15	0.62	3.9[e]	0.44	−9.3	+0.9	Gl(49), Plag(32), Opx(4), Cpx(12), Mt(3), Qu	0.09	<1
				Run 6, 4060 bars, 1000°C, f_{H2} = 0.5 bar, 32 hours				
HAB20	1.00	8.3[f]	0.90	−6.7	+3.4	Gl(92), Cpx(3), Mt(5)	0.26	<1
HAB21	0.64	5.0[e]	0.63	−7.0	+3.1	Gl(39), Plag(38), Opx(5), Cpx(12), Mt(6)	0.03	<1
				Run 7, 4058 bars, 1025°C, f_{H2} = 0.3 bar, 13 hours				
HAB23	1.00	8.3[f]	0.92	−5.9	+3.8	Gl(95), Mt(5)	0.57	<1
HAB24	0.81	5.8[e]	0.66	−6.2	+3.5	Gl(65), Plag(19), Cpx(10), Mt(6)	0.11	<1
HAB25	0.60	2.6[e]	0.22	−7.2	+2.5	Gl(43), Plag(36), Opx(5), Cpx(9), Mt(7)	0.06	<1
				Run 8, 3988 bars, 952°C, f_{H2} = 0.3 bar, 58 hours				
P1D[h]	1.00	7.9[f]	0.95	−7.0	+3.9	Gl(96), Mt(4)	0.31	<1

[a] $XH_2Oin.$, initial $H_2O/(H_2O + CO_2)$ in the charge; aH_2O calculated from H_2O in glass using the model of *Burnham* [1979]; log f_{O2} calculated from experimental f_{H2} (see text) and calculated f_{H2O} (obtained from aH_2O);ΔNNO = log f_{O2} - log f_{O2} of the NNO buffer calculated at P and T [*Chou*, 1987]; nd, not determined (glass pools too small for analysis).

[b] Phase proportions calculated by mass balance; Gl, glass; Plag, plagioclase; Opx, orthopyroxene; Cpx, clinopyroxene; Mt, magnetite; Ilm, ilmenite; Amph, amphibole; Ol, olivine; Qu, quench crystals detected by SEM.

[c] Apparent loss or gain of FeO calculated as 100 (FeOcalc - FeOstarting sample)/FeOstarting sample.

[d] Estimated from average (8.2 ± 0.12 wt %) of Karl-Fischer analyses for the other H_2O-saturated glasses # HAB6, 17, 20, 23.

[e] Estimated using the by-difference method.

[f] Analyzed by Karl-Fischer titration.

[g] Analyzed by FTIR.

[h] Starting composition was andesite MT33S (Table 1). All other experiments run with the basaltic andesite starting composition 031-22b (Table 1).

Crystalline phases in charge HAB25 could not be satisfactorily analyzed because of their small size, and only Cpx compositions are reported (Table 8).

[31] Phase assemblages for ΔNNO < +1 are characterized by the near absence of Fe-Ti oxides. Magnetite is found (with ilmenite) in only one charge from the low end of the experimental temperature range (HAB3, 949°C, Table 7 and Figure 7). In contrast, phase assemblages above NNO +1 all have magnetite present. The magnetite saturation temperature strongly increases with fO_2, from 949°C for ΔNNO < +1, to >995°C for ΔNNO = +1.3 and >1025°C for ΔNNO > +2.5 (Figure 7). Above NNO +1, magnetite is a near-liquidus or a liquidus phase for the basaltic andesite composition (and also for the andesite composition P1D, Table 7, see also *Martel et al.* [1999]). Olivine was found in only one charge (HAB7) suggesting the existence of a very small olivine stability field, not represented in Figure 7. Olivine is present in one of the less oxidized charges (ΔNNO = +0.4). Similarly, ilmenite is restricted to ΔNNO < +0.6. Clinopyroxene is the liquidus phase for ΔNNO < +1 and the second phase in the crystallization sequence for more oxidizing conditions. Under H_2O-saturated conditions it appears between 1025 and 1000°C and is followed by plagioclase + amphibole. At lower temperatures (∼950°C), clinopyroxene reacts out to amphibole-bearing assemblages. Orthopyroxene is found in H_2O-undersaturated charges only. Its stability field progressively shifts toward lower melt H_2O concentrations upon increasing f_{O2} (Figure 7). The amphibole saturation curve shows a temperature maximum between 1000 and 1016°C for a melt H_2O content of ∼7 wt % H_2O [e.g., *Holloway*, 1973; *Ghiorso*, 1999], and amphibole is absent from charges with <5 wt % H_2O in melt (Figure 7).

[32] The compositions of experimental phases show important variations with the intensive parameters (Table 8). The An content in plagioclase increases with increasing melt H_2O at a given temperature (Figure 8). An contents ≥85 are restricted to charges with melt H_2O contents >5 wt %. Compositions up to An_{89} were obtained for H_2O-saturated conditions at 950°C but not at 1000°C because plagioclase is not stable at these temperatures under H_2O-saturated conditions (Figure 7). The Ca/Na partition coefficient between plagioclase and melt $(Ca/Na)_{Plag}/(Ca/Na)_{glass}$ is a strong function of the glass H_2O concentration [e.g., *Sisson and Grove*,

Table 8. Experimental Compositions[a]

Charge	Phase	SiO_2	TiO_2	Al_2O_3	FeO_t	MnO	MgO	CaO	Na_2O	K_2O	Total	mol%
					Run 0, 1 bar, 1400°C, Air, 2 × 4 hours							
HAB0	Gl(4[b])	53.6(4[c])	0.80(5)	19.1(20)	8.14(27)	0.25(7)	4.46(4)	9.85(15)	3.02(3)	0.74(4)	98.1	
					Run 1, 3988 bars, 949°C, f_{H2} = 8.1 bars, 99 hours							
HAB1	Gl(2)	61.7(5)	0.63(1)	17.6(2)	7.30(27)	0.20(25)	1.85(0)	6.40(18)	3.13(25)	1.21(1)	90.4	
	Plag(5)	45.2(5)	0.00(0)	33.9(2)	0.83(19)	0.02(2)	0.04(3)	18.3(2)	1.23(10)	0.02(2)	99.5	$An_{89}Or_0$
	Amph(8)	41.9(5)	1.75(14)	12.9(7)	12.2(6)	0.22(8)	13.4(7)	11.5(3)	2.15(8)	0.33(7)	96.4	
HAB2	Gl(1)	62.1	0.58	17.6	7.12	0.20	1.64	5.75	3.48	1.53	90.2	$An_{73}Or_1$
	Plag(1)	50.1	0.10	29.9	1.80	0.01	0.22	13.8	2.73	0.22	98.9	
	Amph(2)	42.0(2)	2.65(19)	12.2(4)	15.0(7)	0.31(1)	12.2(4)	10.7(2)	2.31(21)	0.37(6)	97.9	
	Opx(1)	51.8	0.33	3.56	22.0	0.78	20.0	2.42	0.08	0.05	101.1	$En_{59}Wo_5$
HAB3	Plag(1)	53.7	0.08	29.3	0.97	0.11	0.15	12.4	3.94	0.36	101.0	$An_{62}Or_2$
	Opx(3)	50.6(5)	0.40(7)	2.43(20)	24.9(4)	0.50(21)	18.6(2)	2.14(51)	0.05(5)	0.03(3)	99.7	$En_{55}Wo_5$
	Cpx(2)	50.8(1)	0.69(5)	6.37(133)	12.1(79)	0.37(25)	10.9(10)	17.1(0)	0.76(17)	0.16(3)	99.22	$En_{36}Wo_{41}$
	Mt(1)	1.09	14.9	3.85	70.1	0.42	1.98	0.33	0.02	0.03	92.7	Mt_{49}
	ilm(1)	1.08	46.0	0.81	45.6	0.31	2.46	0.59	0.05	0.03	96.9	Hm_{11}
					Run 2, 4270 bars, 1000°C, f_{H2} = 14.3 bars, 40 hours							
HAB6	Gl(6)	53.4(3)	0.83(6)	19.3(2)	8.23(39)	0.21(12)	4.31(31)	9.56(34)	3.36(10)	0.78(8)	88.0	
	Cpx(3)	50.1(3)	0.57(8)	4.17(41)	6.63(28)	0.21(9)	14.5(4)	22.1(4)	0.20(2)	0.03(2)	98.9	$En_{43}Wo_{46}$
HAB7	Gl(2)	56.4(5)	0.85(4)	18.7(2)	8.36(39)	0.04(1)	3.52(6)	7.44(23)	3.74(17)	0.94(7)	91.1	
	Plag(1)	47.2	0.08	32.7	0.84	0.00	0.18	16.5	1.72	0.08	99.5	$An_{84}Or_1$
	Amph(3)	42.8(10)	2.32(26)	13.1(5)	11.5(9)	0.18(10)	13.6(10)	10.8(4)	2.33(4)	0.38(2)	97.0	
	Cpx(1)	49.4	0.76	5.78	9.47	0.43	13.54	19.36	0.44	0.08	99.3	$En_{41}Wo_{43}$
	ol(3)	37.5(1)	0.02(3)	0.04(5)	27.2(6)	0.49(12)	34.7(3)	0.18(4)	0.01(2)	0.00(0)	100.1	Fo_{69}
HAB8	Gl(3)	58.1(3)	1.41(5)	17.5(4)	9.84(35)	0.17(6)	2.60(18)	6.21(14)	2.71(20)	1.41(1)	92.5	
	Plag(1)	50.4	0.10	30.0	1.02	0.01	0.17	14.1	3.16	0.17	99.1	$An_{70}Or_1$
	Opx(4)	50.3(2)	0.49(2)	4.24(55)	20.4(9)	0.38(9)	20.7(4)	2.28(23)	0.13(9)	0.04(3)	98.9	$En_{61}Wo_5$
	Cpx(2)	49.4(10)	0.87(4)	4.60(11)	13.5(9)	0.38(25)	14.1(2)	16.8(6)	0.32(2)	0.08(5)	100.2	$En_{42}Wo_{36}$
					Run 3, 3949 bars, 1016°C, f_{H2} = 9.7 bars, 22 hours							
HAB17	Gl(4)	53.9(7)	0.86(13)	19.0(4)	8.36(31)	0.19(11)	4.31(10)	9.58(11)	3.10(31)	0.75(4)	89.8	
HAB18	Gl(4)	53.7(5)	0.88(8)	18.7(2)	8.30(24)	0.13(2)	4.52(4)	9.46(7)	3.50(8)	0.83(4)	92.7	
	Plag(1)	46.7	0.00	33.6	0.92	0.00	0.13	18.2	1.67	0.02	101.2	$An_{86}Or_0$
	Cpx(2)	48.7(1)	0.69(5)	6.09(94)	8.18(39)	0.26(5)	14.0(8)	20.5(1)	0.42(15)	0.08(5)	98.94	$En_{42}Wo_{44}$
HAB19	Gl(4)	55.7(6)	1.01(10)	17.7(4)	9.66(36)	0.18(6)	3.64(7)	7.71(2)	3.19(24)	1.16(4)	93.9	
	Plag(1)	50.1	0.04	31.6	0.90	0.09	0.10	14.8	3.22	0.07	100.9	$An_{72}Or_0$
	Opx(6)	52.8(9)	0.27(7)	3.15(109)	16.7(6)	0.39(7)	24.4(8)	2.19(39)	0.07(8)	0.02(3)	100	$En_{69}Wo_5$
	Cpx(3)	49.8(9)	0.80(12)	5.72(29)	10.9(5)	0.22(11)	14.3(6)	17.5(9)	0.43(9)	0.06(7)	99.8	$En_{43}Wo_{38}$
					Run 4, 4002 bars, 945°C, f_{H2} = 4.6 bars, 60 hours							
HAB11	Gl(3)	61.1(8)	0.55(7)	19.5(3)	5.32(7)	0.20(6)	1.71(8)	7.53(13)	2.92(7)	1.11(12)	87.9	
	Plag(2)	46.7(2)	0.03(3)	33.8(0)	0.76(11)	0.00(0)	0.08(4)	18.0(2)	1.30(24)	0.06(4)	100.8	$An_{88}Or_0$
	Amph(3)	42.6(6)	1.85(27)	13.2(3)	12.5(9)	0.28(14)	13.6(1)	11.3(2)	2.14(12)	0.35(2)	97.8	
	Mt(2)	0.20(8)	4.43(8)	5.61(3)	81.4(0)	0.42(5)	3.12(3)	0.26(3)	0.03(4)	0.02(1)	95.5	Mt_{87}
HAB12	Gl(3)	64.5(12)	0.46(8)	18.0(4)	5.11(63)	0.19(3)	1.49(26)	5.62(12)	3.17(35)	1.47(1)	91.0	
	Plag(2)	49.9(5)	0.05(6)	31.4(12)	1.06(19)	0.03(4)	0.15(8)	15.5(5)	2.54(22)	0.19(12)	100.8	$An_{76}Or_1$
	Amph(2)	43.8(2)	1.87(4)	11.9(6)	12.2(1)	0.14(2)	14.1(1)	11.2(4)	2.17(0)	0.33(5)	97.6	
	Mt(2)	0.23(4)	5.44(13)	5.19(10)	80.7(5)	0.51(4)	2.67(11)	0.37(9)	0.01(1)	0.03(4)	95.1	Mt_{83}

Table 8. (continued)

Charge	Phase	SiO_2	TiO_2	Al_2O_3	FeO_t	MnO	MgO	CaO	Na_2O	K_2O	Total	mol%
					Run 4, 4002 bars, 945°C, f_{H2} = 4.6 bars, 60 hours							
HAB13	Plag(1)	51.3	0.19	29.3	0.98	0.00	0.13	13.1	3.64	0.19	98.9	$An_{66}Or_1$
	Opx(2)	53.2(2)	0.34(11)	3.18(8)	17.2(7)	0.72(2)	24.7(2)	1.48(13)	0.06(1)	0.02(3)	100.9	$En_{70}Wo_3$
	Cpx(1)	51.9	0.54	4.42	14.6	0.59	18.7	10.0	0.43	0.10	101.3	$En_{55}Wo_{21}$
	Mt(1)	0.86	9.76	4.23	77.6	0.56	2.47	0.38	0.01	0.03	95.9	Mt_{69}
					Run 5, 4048 bars, 995°C, f_{H2} = 4.3 bars, 49 hours							
HAB14	Gl(3)	56.9(10)	0.78(8)	18.9(4)	7.65(33)	0.15(12)	3.50(29)	8.30(41)	3.21(12)	0.59(9)	91.5	
	Plag(2)	47.5(4)	0.00(0)	33.2(8)	0.92(2)	0.00(0)	0.10(13)	17.4(6)	1.66(35)	0.08(8)	100.9	$An_{85}Or_0$
	Amph(3)	43.0(4)	2.01(7)	12.9(6)	11.5(10)	0.16(15)	14.8(2)	11.2(1)	2.22(9)	0.32(3)	98.0	
	Cpx(3)	49.0(5)	0.78(13)	5.92(32)	10.0(5)	0.39(6)	14.5(4)	19.1(9)	0.39(9)	0.04(5)	100.2	$En_{43}Wo_{40}$
	Mt(2)	0.46(13)	4.68(33)	7.84(19)	77.1(8)	0.34(5)	4.47(8)	0.34(10)	0.05(7)	0.06(1)	95.3	Mt_{85}
HAB15	Gl(2)	60.2(1)	0.80(16)	17.7(2)	7.06(4)	0.12(6)	2.67(0)	6.39(4)	3.49(14)	1.59(8)	93.4	
	Plag(1)	50.7	0.17	29.5	1.22	0.04	0.25	13.9	3.10	0.15	99.1	$An_{71}Or_1$
	Opx(6)	52.7(5)	0.28(5)	3.85(100)	15.7(9)	0.54(6)	25.0(9)	2.03(61)	0.10(9)	0.01(2)	100.2	$En_{71}Wo_4$
	Cpx(1)	49.0	0.73	5.05	11.2	0.41	15.2	16.8	0.28	0.02	98.8	$En_{46}Wo_{36}$
	Mt(1)	0.73	7.09	5.68	76.8	0.22	3.33	0.37	0.02	0.01	94.2	Mt_{77}
					Run 6, 4060 bars, 1000°C, f_{H2} = 0.5 bar, 32 hours							
HAB20	Gl(4)	57.0(6)	0.45(6)	20.3(2)	3.09(14)	0.24(7)	4.36(6)	9.86(9)	3.75(6)	0.91(5)	89.0	
	Cpx(4)	43.6(6)	0.96(22)	9.23(39)	9.67(20)	0.04(4)	11.4(3)	23.6(2)	0.33(5)	0.03(2)	98.9	$En_{34}Wo_{50}$
	Mt(1)	0.08	6.47	2.26	81.7	0.00	2.38	0.10	0.07	0.01	93.1	Mt_{81}
HAB21	Gl(3)	66.9(6)	0.41(7)	16.6(4)	2.83(36)	0.15(3)	2.16(10)	4.96(16)	3.99(34)	2.00(5)	93.1	
	Plag(1)	50.5	0.06	30.2	1.27	0.00	0.16	14.1	3.53	0.17	99.9	$An_{68}Or_1$
	Opx(1)	54.0	0.21	4.89	8.14	0.86	29.8	1.58	0.12	0.08	99.7	$En_{84}Wo_3$
	Cpx(1)	49.1	0.85	5.45	8.80	0.40	15.0	19.7	0.41	0.00	99.8	$En_{44}Wo_{42}$
	Mt(1)	1.13	7.26	2.39	77.3	0.24	2.37	0.36	0.09	0.00	91.1	Mt_{77}
					Run 7, 4058 bars, 1025°C, f_{H2} = 0.3 bar, 13 hours							
HAB23	Gl(4)	56.2(6)	0.58(7)	20.0(1)	3.89(24)	0.22(9)	4.29(6)	10.1(2)	3.88(8)	0.87(5)	90.2	
	Mt(2)	0.12(5)	6.03(34)	2.29(6)	78.4(5)	0.18(8)	2.58(14)	0.12(1)	0.02(3)	0.04(1)	89.8	Mt_{82}
HAB24	Gl(3)	61.3(3)	0.43(4)	18.6(1)	3.50(25)	0.15(12)	3.84(6)	7.09(21)	4.02(14)	1.12(2)	92.2	
	Plag(2)	48.8(0)	0.01(1)	31.6(3)	1.18(11)	0.00(0)	0.17(3)	16.1(7)	2.45(36)	0.06(1)	100.3	$An_{78}Or_0$
	Cpx(3)	47.3(8)	0.63(13)	6.79(23)	7.91(109)	0.38(10)	14.3(4)	21.1(5)	0.44(3)	0.05(4)	99	$En_{42}Wo_{45}$
	Mt(2)	0.47(53)	6.66(14)	2.54(19)	77.2(2)	0.16(22)	2.61(10)	0.26(19)	0.06(8)	0.01(1)	90	Mt_{80}
HAB25	Gl(1)	62.2	0.28	19.5	2.51	0.17	2.42	7.94	3.67	1.36	95.9	
	Cpx(1)	49.8	0.71	6.32	7.35	0.37	15.0	20.4	0.47	0.07	100.5	$En_{44}Wo_{43}$
					Run 8, 3988 bars, 952°C, f_{H2} = 0.3 bar, 58 hours							
P1D	Gl(4)	64.5(7)	0.25(7)	17.8(10)	2.90(12)	0.17(10)	2.29(3)	6.69(14)	4.25(6)	1.11(7)	90.7	
	Mt(2)	0.09(3)	5.83(46)	1.76(16)	83.0(3)	0.02(3)	1.11(5)	0.10(6)	0.02(3)	0.02(3)	92.0	Mt_{80}

[a] Glass analyses normalized to 100% anhydrous, with all Fe as FeO. Original unnormalized total is reported. For HAB25, analyses of Plag, Opx, and Mt are of poor quality (crystals too small) and are not reported. Abbreviations are as in Table 7.

[b] Number of microprobe analyses.

[c] One standard deviation in terms of least unit cited.

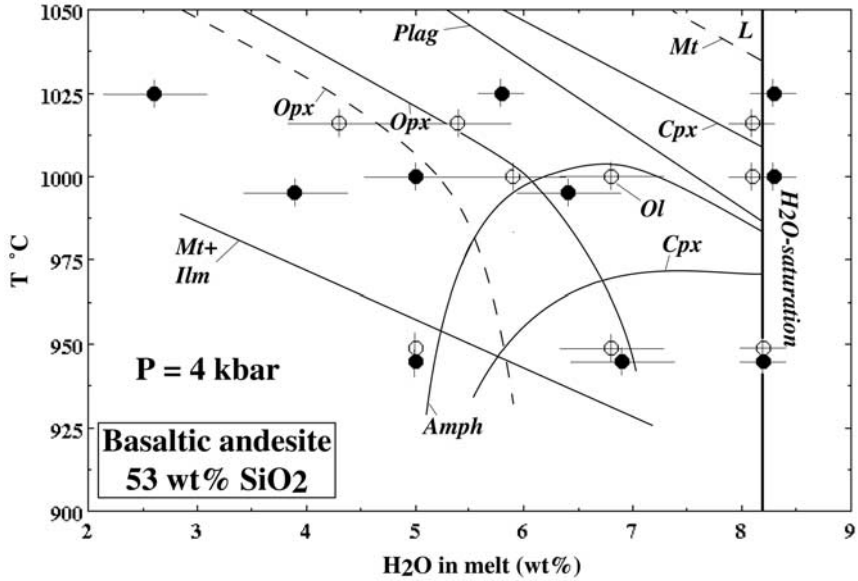

Figure 7. Phase relations for the basaltic andesite from Grand Rivière at 4 kbar. Data and abbreviations are from Table 7. Experimental data points for the different f_{O2} investigated are plotted together: open circles, ΔNNO < +1; solid circles, +1< ΔNNO < +1.5 and ΔNNO > +2.5. Stability curves labeled with mineral names inside their stability field. Cpx (both in and out curves), Plag, and Amph saturation curves (independent on f_{O2}) are shown as solid lines. For Fe-Ti oxides the influence of f_{O2} on saturation curves is marked; the Fe-Ti oxide saturation curve for ΔNNO < +1 is shown as a solid line. Notice that Ilm coexists with Mt. For ΔNNO > +2.5 the Mt saturation curve (dashed line) has not been bracketed and is shown for illustration purposes only to indicate that Mt is the liquidus phase under these f_{O2} conditions. For Opx the solid line corresponds to Opx saturation for ΔNNO < +1, and the dashed line corresponds to ΔNNO > +2.5. Although no Ol stability field has been represented, Ol is present in one charge at 1000°C. The melt H_2O content of the two less water-rich charges at 949 and 945°C (HAB3 and HAB13, Table 7) is unknown and has been estimated at 5 wt % for the construction of the diagram.

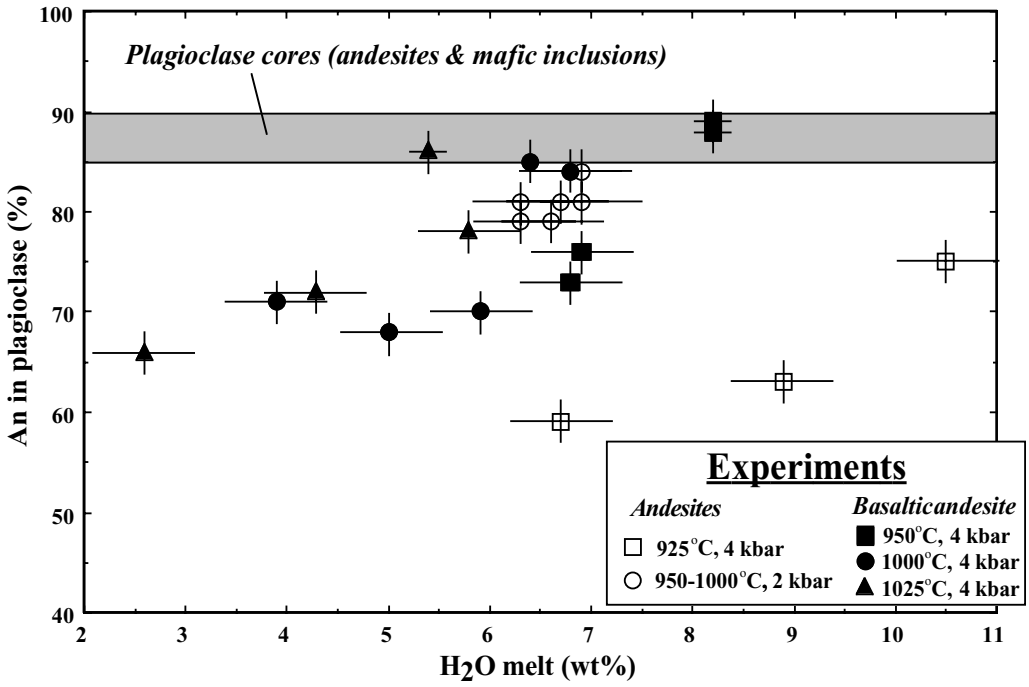

Figure 8. Compositions of plagioclases in the basaltic andesite (Table 8) and andesite experiments [*Martel et al.*, 1999] plotted as a function of the H_2O content of the coexisting melt. Each experimental data point represents the average composition of plagioclase in a given charge. The average compositions of plagioclase cores in andesites and mafic enclaves from stage 3 are shown for comparison. Note that experiments designated as 950°C correspond to charges at both 949 and 945°C, as 1000°C to charges at both 1000 and 995°C and as 1025°C to charges at both 1025 and 1016°C (Table 7). Charges with different f_{O2} plotted with the same symbol (see Table 7).

1993a]. At 1000°C it is 3.2 for 5 wt % H_2O, 4.1 for 6.4 wt %, and 4.8 for 6.8 wt % (data in Table 8), in good agreement with published values for comparable T-H_2O and bulk compositions (~5.5, from *Sisson and Grove* [1993a] and 3.9–4.5, from *Grove et al.* [1997], both for ~6 wt % H_2O). Olivine in charge HAB7 is Fo_{69}, yielding a Fe/Mg olivine-melt partition coefficient $(Fe/Mg)_{Ol}/(Fe/Mg)_{glass}$ of 0.33 (total Fe as FeO), within the range of previous studies (0.28 ± 0.05, from *Sisson and Grove* [1993a] and 0.30 ± 0.05, from *Grove et al.* [1997]). Orthopyroxenes ($En_{59-84}Wo_{3-5}Fs_{15-36}$) have Al_2O_3 up to ~5 wt % and Al(IV) up to 0.11 pfu. Increasing f_{O2} at approximately constant T and melt H_2O content increases Mg/(Mg + total Fe) in Opx. The Fe/Mg partition coefficient between orthopyroxene and melt calculated for four charges with f_{O2} < NNO + 1.5 is 0.25 ± 0.01, within the range of previous studies (0.29 ± 0.16, from *Grove et al.* [1997]). Clinopyroxenes ($En_{34-55}Wo_{21-50}Fs_{11-24}$) include salites and augites. Their Wo content increases with increasing melt H_2O content [*Gaetani et al.*, 1993]. They have high Al_2O_3 and Al(IV) values (0.09–0.32). Al(VI) values are nearly constant, 0.10 on average, and Na_2O and TiO_2 are <1 wt %. Charges with ΔNNO < +1.5 yield a Fe/Mg partition coefficient between clinopyroxene and melt of 0.28 ± 0.03 (seven mineral-melt pairs), in good agreement with previous results (0.23–0.27, from *Sisson and Grove* [1993a] and 0.25 ± 0.09, from *Grove et al.* [1997]). For charges above ΔNNO > +2.5 a substantial proportion of Fe is incorporated in Cpx as $CaFe^{3+}AlSiO_6$, leading to an increase of the Fe/Mg partition coefficient calculated with all Fe as Fe^{2+}. Magnetites (Mt_{49-87}) are Al_2O_3-rich (up to nearly 8 wt %) and magnesian (Mg # calculated with Fe as Fe^{2+} up to ~0.2). They have TiO_2 contents between 4 and 10 wt % and proportions of Fe as Fe^{3+} mostly between 50 and 60%. Amphiboles are pargasitic hornblendes with Al(IV) = 1.7–1.8, number of cations in site A of 0.65–0.75 pfu and Mg # (calculated with total Fe as FeO) mostly between 0.65 and 0.70. They have TiO_2 contents between 1.7 and 2.7 wt % and Na_2O contents between 2.1 and 2.3 wt %. The Fe/Mg partition coefficient between amphibole and melt progressively varies with the composition of the coexisting melt [*Sisson and Grove*, 1993a]. It is 0.27 ± 0.03 (four charges) for melt SiO_2 > 61 wt % and 0.36 ± 0.00 (two charges) for melt SiO_2 = 56 wt %, in excellent agreement with previous values for basaltic andesite to andesite melts (0.30–0.38, from *Sisson and Grove* [1993a] and *Grove et al.* [1997]). For comparison, the Fe/Mg partition coefficient is 0.12 ± 0.02 for amphibole coexisting with a rhyolitic melt [*Martel et al.*, 1999]. The six amphibole-melt mineral pairs from this study define an Al-Si partition coefficient $(Al/Si)_{Amph}/(Al/Si)_{glass}$ of 0.97 ± 0.06, independent on melt composition and identical within error to the value thought to apply from high-alumina basalt to rhyolite (0.94, from *Sisson and Grove* [1993a]). Experimental glasses range continuously from basaltic andesite through andesite to dacite. With progressive crystallization, glasses become enriched in SiO_2, K_2O, and Na_2O, while Al_2O_3, MgO, and CaO decrease (Figure 9). Oxygen fugacity controls the proportion of magnetite present, TiO_2, FeO_t, and FeO_t/MgO for a given SiO_2 content, making liquid compositions strongly dependent on f_{O2} (Figure 9, see also *Sisson and Grove* [1993a]). Liquids produced under very oxidizing conditions (ΔNNO > +2.5) have FeO_t/MgO that are equal or decrease with progressive crystallization (Figure 9), which indicates preferential partitioning of Fe toward the mineral phases relative to Mg.

5. Discussion

[33] One of the important characteristics of the activity of Mount Pelée during the second and third stages is the constant presence of mafic compositions [*Bourdier et al.*, 1985; *Fichaut et al.*, 1989a; *Gourgaud et al.*, 1989; *Villemant et al.*, 1996]. The second stage of activity is dominated by eruption products of dominantly basaltic andesite composition. Typical eruptive sequences include andesitic deposits successively overlain by banded pumices and finally thick basaltic andesite to basaltic deposits which may contain gabbroic cumulate blocks [*Bourdier et al.*, 1985; *Fichaut et al.*, 1989b]. During the recent period, no basaltic andesite erupted as a lava, but the presence of mafic compositions in the magma storage zone is attested to by the conspicuous occurrence of mafic enclaves in andesites [*Gourgaud et al.*, 1989]. Whole rock compositions of mafic enclaves and mafic lavas overlap (Figure 2), suggesting that enclaves of the recent period represent samples of mafic magmas similar to the lavas erupted during stage 2 (see *Bacon* [1986] for a similar case at Mount Mazama). The evidence coming from the last 40,000 years of activity of the volcano thus establishes the presence of mafic magmas beneath Mount Pelée, even if all the most recently erupted products have andesite bulk compositions. Therefore the magma storage zone must be viewed as a compositionally zoned igneous system, with a mafic part and an andesitic part. Below, we use the experimental data together with data on eruption products to constrain the preeruptive conditions in the andesitic and mafic parts of the magma chamber.

5.1. Andesitic Part

5.1.1. Experimental constraints. [34] *Martel et al.* [1998] have compared compositions of phenocryst rims and interstitial glasses of recent andesites with experimental compositions from andesite run products [*Martel et al.*, 1999] to constrain the conditions in the upper andesitic part of the magma chamber. Their results are summarized on Figure 10. The determined preeruptive temperature is between 875 and 900°C, overlapping with, but slightly higher than, the new Fe-Ti oxide data (848–880°C, see above) and the average pyroxene temperatures (850 and 870°C for Opx and Cpx respectively, see above). A pressure of 2 ± 0.5 kbar was estimated for the andesitic magma body tapped by recent eruptions. Redox conditions (ΔNNO = +0.4–0.8) are in good agreement with the new Fe-Ti oxide data (ΔNNO = +0.3–0.5). The range of melt H_2O content (5.3–6.3 wt %) encloses the average H_2O concentration of glass inclusions in the Plinian fallout (5.8 wt %, see above and *Martel et al.* [2000]) and corresponds to aH_2O values of 0.8–0.9 [*Martel et al.*, 1999]. Experiments under these P-T-f_{O2}-H_2O melt reproduce the main assemblage and modal proportions of phenocrysts (Plag + Opx + Mt) in recent andesites [*Martel et al.*, 1998, 1999] and therefore model the main stage of crystallization of magmas in the andesitic part of the chamber. Phenocryst rim and interstitial glass compositions are nearly identical for the P1, 1902, and 1929 eruptions (see above), suggesting that preeruptive conditions in the andesitic part varied little between eruptions studied and, in particular, were the same for Plinian and Pelean eruptions. Therefore, during the last part of the recent period the andesitic part of the chamber has been evolving under stable or steady state conditions, consistent with the bulk chemical homogeneity of products erupted during that period.

[35] There are, however, some mineralogical features of recent products that are not accounted for by the andesite experiments. First, olivine was never encountered in run products, whatever the starting composition investigated [*Martel et al.*, 1999]. Second, plagioclase compositions as calcic as the plagioclase cores were not obtained. The most calcic plagioclases in the andesite experiments (An_{84}) are for H_2O-saturated conditions at 2 kbar, 950 and 1000°C (Figure 10). Less calcic compositions crystallized at 4 kbar, 925°C, suggesting that plagioclases with compositions such as the calcic cores (average An_{85-90}, values up to An_{94}, see above) crystallized from bulk compositions more calcic than those investigated by *Martel et al.* [1999]. Third, the experiments did not produce pargasitic hornblende compositions as most amphibole phenocrysts. Amphiboles with the highest Al(IV) were obtained at 4 kbar, but these still show important differences with the natural pargasitic hornblendes (e.g., Mg #, Figure 11). At 2 kbar, 876°C, experimental amphiboles crystallized under aH_2O = 1 (i.e., under conditions very close to the andesitic part of the chamber, Figure 10) have edenitic

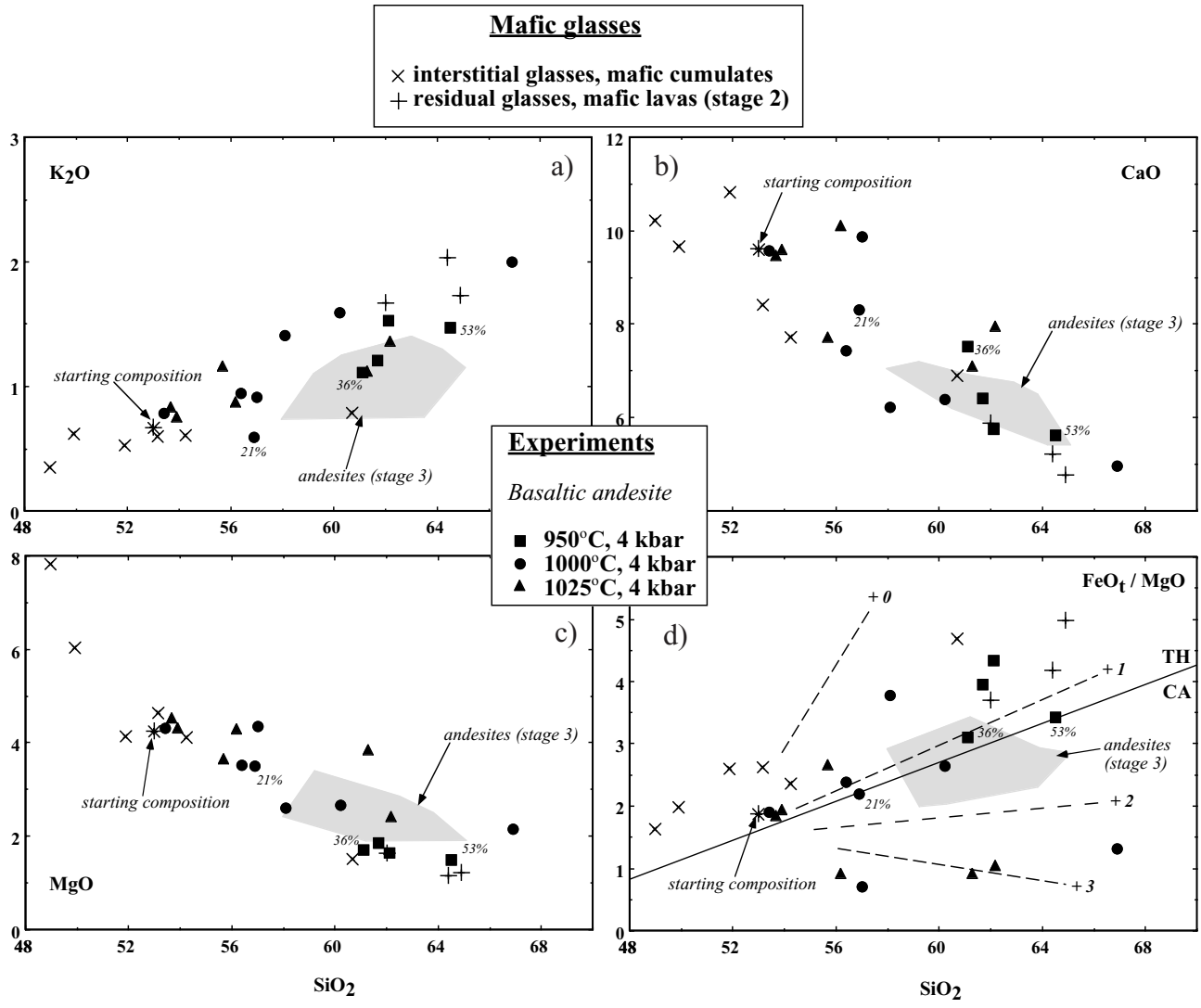

Figure 9. SiO_2 variation diagrams for (a) K_2O, (b) CaO, (c) MgO, and (d) FeO_t/MgO [*Miyashiro*, 1974] for the experimental glasses, normalized to 100% anhydrous. Data and uncertainties are given in Table 8. Experimental charges are grouped as in Figure 8. Charges with different f_{O2} are plotted with the same symbol (see Table 7). Experimental glasses are compared with compositions of mafic glasses in mafic cumulates and lavas (all stage 2 products) from *Bourdier et al.* [1985] and *Fichaut et al.* [1989a, 1989b]. Field of recent (stage 3) andesites (P1, 1902, and 1929 eruption products, see Figure 2) is shown for reference. In Figure 9d the dashed lines represent ΔNNO contours for charges with melt H_2O contents in the range 6–8 wt %. Proportions (wt %) of crystals are shown for three magnetite-bearing charges (HAB11, HAB12, and HAB14, Table 7) with f_{O2} in the same range (ΔNNO = +1.2–1.3) and H_2O contents in the range 6–8 wt % to illustrate the effect of progressive crystallization on melt composition. TH, tholeiitic field; CA, calk-alkaline field.

compositions (Figure 11), which demonstrates that the pargasitic hornblendes are not crystallization products from the andesitic magma body. Fourth, clinopyroxenes in the andesite experiments are Al-poor and differ from compositions of some Al-, Fe^{3+}-rich Cpx found in andesites (Figure 12). Aluminous magnetites such as found in reaction rims have not been reproduced in the andesite experiments. Therefore the experiments demonstrate the presence in recent eruption products of a population of crystals (calcic Plag, Ol, pargasitic Amph, Al-rich Cpx, aluminous Mt) that are out of equilibrium with the andesite magma and that were interpreted as xenocrysts in earlier petrological studies [*Fichaut et al.*, 1989a; *Gourgaud et al.*, 1989]. It is stressed that the proportion of such phases in P1, 1902, and 1929 andesites is small and largely dominated by the calcic plagioclase cores. Olivine and pargasitic hornblende only make up a very small proportion of phenocrysts in eruption products. Nevertheless, models of closed-system crystallization of andesite liquids do not explain all the mineralogical characteristics of the andesitic part of the chamber.

5.1.2. Amphibole stability in the andesitic part. [36] The amphibole saturation curve for $aH_2O = 1$ intersects the preeruptive P-T domain for the andesitic magma body (Figure 10). However, for $aH_2O < 1$, corresponding to the range of preeruptive melt H_2O concentrations (i.e., $aH_2O = 0.8–0.9$, see above), the amphibole saturation curve progressively shifts toward lower temperatures and higher pressures [*Martel et al.*, 1999]. Therefore the P-T-H_2O melt conditions for the andesitic part lie close to but outside the stability field of amphibole (Figure 10), indicating that amphibole should not crystallize as a stable phase in the upper part of the chamber. This is consistent with petrographic evidence: Amphibole is present in very low modal proportions in recent Mount Pelée andesites; amphibole

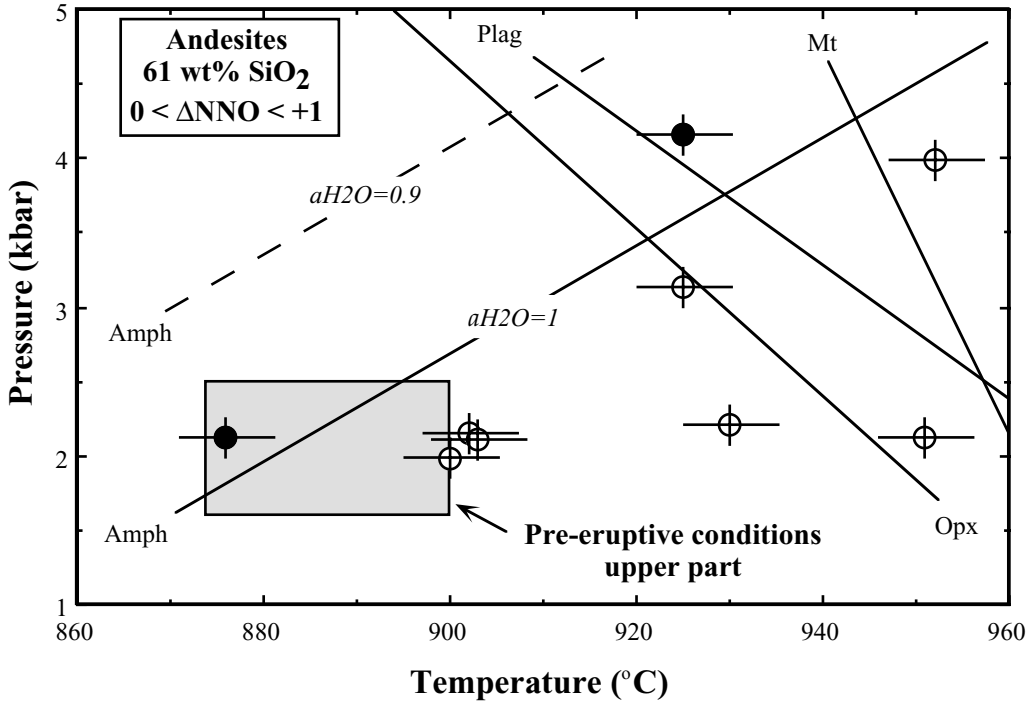

Figure 10. Summary P-T diagram showing Mount Pelée andesite phase equilibria for $aH_2O = 1$ (solid) and 0.9 (dashed, for amphibole only). All experimental data points are for $0 < \Delta NNO < +1$ [*Martel et al.*, 1999] except the 950°C, 4 kbar point ($\Delta NNO = +3.9$, Table 7). Amphibole is stable only at 876°C, 2 kbar and 925°C, 4 kbar for $aH_2O = 1$ (solid symbols). It is unstable for $aH_2O < 1$ and for all other P-T conditions, irrespective of aH_2O (open symbols). The box shows the determined preeruptive P-T conditions in the andesitic part of the magma chamber [*Martel et al.*, 1998]; see also text. Abbreviations are as in Table 7.

textures indicate resorption to Plag + Opx + Mt. However, the fact that amphiboles with and without reaction rims coexist implies that it was originally stable and later underwent resorption. One important observation is that Plinian products (i.e., erupted on the order of hours) have amphiboles with thick (up to several 100 μm) reaction rims. According to kinetic studies of amphibole resorption in magmas [*Rutherford and Hill*, 1993], such textures cannot be obtained for short reaction times and require durations much longer than magma ascent in Plinian-type eruptions. Since amphibole textures are the same in Plinian and Pelean products, it is concluded that amphibole resorption is not related to syneruptive magma ascent but occurs as a response to changing magmatic conditions at depth. Amphibole is thus stable in certain regions of the magma storage system and unstable in other (Figure 10).

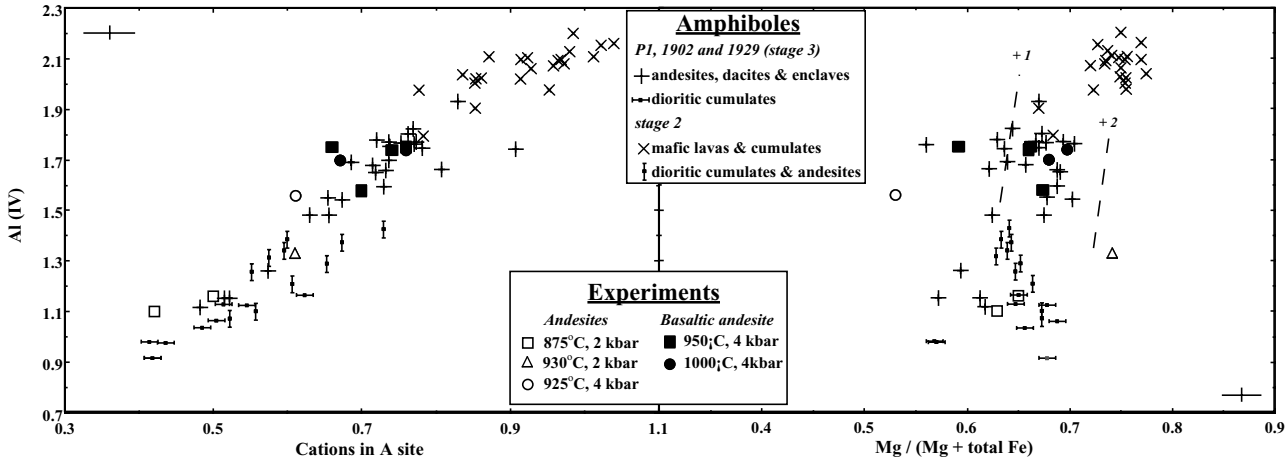

Figure 11. Compositions of experimental amphiboles and comparison with natural amphiboles from stage 2 and 3 eruption products. Structural formulae are calculated on a 23 O basis with all Fe as FeO. Data are from Table 8 for the basaltic andesite and *Martel et al.* [1999] for the andesite experiments. Each experimental data point represents the average composition of amphibole in a given charge. For the basaltic andesite data points, experimental charges are grouped as in Figure 8. Charges with different f_{O2} are plotted with the same symbol. Dashed lines are ΔNNO contours constructed from data in Table 7. Compositions of natural amphiboles are from this study and from *Bourdier et al.* [1985], *Fichaut et al.* [1989a, 1989b], and *Gourgaud et al.* [1989]. Error bars are shown as crosses (top left and bottom right).

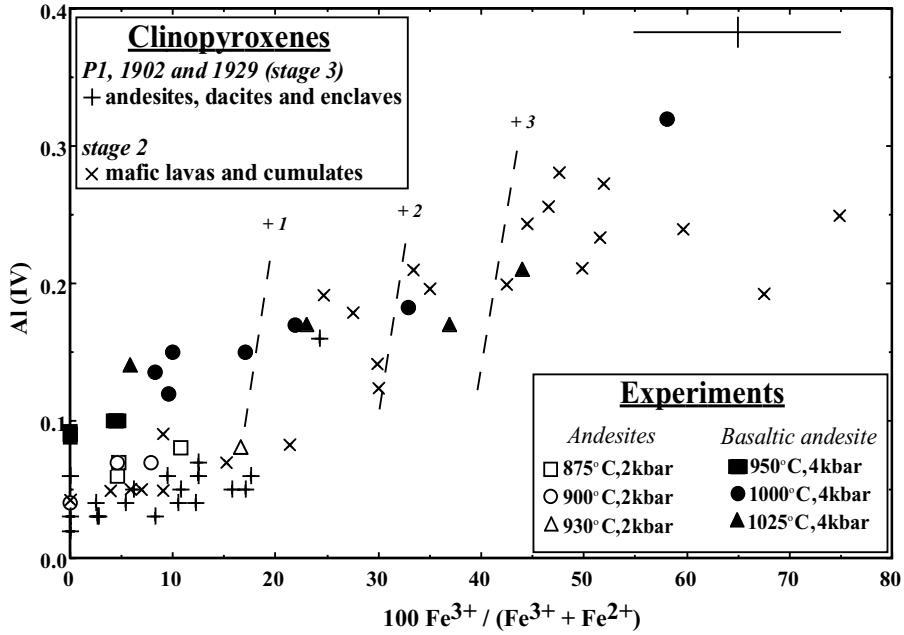

Figure 12. Compositions of experimental clinopyroxenes and comparison with natural clinopyroxenes from stage 2 and 3 eruption products. Structural formulae are calculated on a 6 oxygen basis. Data are from Table 8 for the basaltic andesite and *Martel et al.* [1999] for the andesite experiments. Each experimental data point represents the average composition of clinopyroxene in a given charge. For the basaltic andesite data points, experimental charges are grouped as in Figure 8. Charges with different f_{O2} are plotted with the same symbol. Dashed lines are ΔNNO contours constructed from data in Table 7. Compositions of natural clinopyroxenes are from this study, *Bourdier et al.* [1985], *Fichaut et al.* [1989a, 1989b], and *Gourgaud et al.* [1989]. Note the large uncertainty (cross) on the proportion of Fe^{3+}.

[37] It is interesting to note that the edenitic amphiboles from rare evolved 1902 and 1929 lavas and dioritic cumulates have compositions in the same range as experimental amphiboles at 876°C, 2 kbar, $aH_2O = 1$ (Figures 6 and 11). Application of the Fe/Mg and Al/Si partition coefficients (0.12 and 0.97, respectively, see above) shows that this group of amphiboles crystallized at equilibrium with melts having Mg # between 14 and 21 and Al/Si between 0.17 and 0.22, i.e., identical or slightly more evolved than the interstitial glasses (Mg # = 19–22, Al/Si = 0.19–0.22, Table 6). These edenitic amphiboles are therefore interpreted as crystallization products of small batches of magmas at temperatures slightly colder (≤850°C at 2 kbar from amphibole stability curves of Figure 10) than the main mass of the andesitic body, possibly along chamber walls or roof [*Fichaut et al.*, 1989a, 1989b]. These are the only amphiboles crystallizing in the andesitic part of the Mount Pelée magma chamber during the recent period. Their occurrence in rare and specific lava compositions (>63 wt % SiO_2) and lithologies (dioritic cumulates) shows that they clearly represent the exception rather than the rule and strengthens the above conclusion about the instability of amphibole in the andesitic part.

[38] Edenitic amphiboles are also found in stage 2 products (Figure 11). Compositions in "old" dioritic cumulates are not very different from those in the recent ones. They yield melt Mg # (~19 on average) and Al/Si values (~0.22 on average) in the same range as compositions of interstitial glasses from the recent period. In contrast, edenitic amphiboles from andesitic deposits coerupted with the basaltic andesite ash-and-scoria flows [*Bourdier et al.*, 1985] are significantly more aluminous and imply crystallization from a melt with Al/Si = 0.25–0.28 or 67–70 wt % SiO_2, i.e., rhyodacitic, a composition not yet detected among natural glasses.

5.2. Mafic Part

[39] Information on the mafic part of the chamber comes from mafic enclaves erupted during stage 3 and from mafic lavas (ash-and-scoria flows) and gabbroic cumulates from stage 2. Mafic enclaves have phenocryst compositions differing relatively little from phenocrysts in andesites (Figures 4–6, 12, and 13), probably because they were hybridized [e.g., *Coulon et al.*, 1984; *Bacon*, 1986; *Clynne*, 1999]. Mafic lavas from stage 2 also carry a minor andesite "component" [*Bourdier et al.*, 1985], but these, together with gabbroic cumulates, appear to preserve phenocryst and glass compositions representative of the mafic part of the system (Tables 2–5 and see below). Gabbroic cumulates from Mount Pelée are similar to those previously described along the Lesser Antilles arc [*Lewis*, 1973; *Arculus and Wills*, 1980; *Bourdier et al.*, 1985; *Fichaut et al.*, 1989b].

5.2.1. Parental mafic magmas. [40] Experimental results for the basaltic andesite composition show that Cpx, Ol, Mt (for appropriate f_{O2}), Plag, and Amph all crystallize together on or near the liquidus in the H_2O-rich part of the diagram (Figure 7). Salitic clinopyroxene is confirmed to be the liquidus phase in hydrous basaltic andesite melts below 5 kbar and for $f_{O2} \geq$ NNO [*Cawthorn et al.*, 1973; *Graham*, 1981]. Magnetite is a liquidus or near-liquidus phase for ΔNNO > +1 but not for 0 < ΔNNO < +1 (Figure 7). Both high f_{O2} and H_2O-rich conditions are needed to stabilize magnetite on or near the liquidus of basaltic liquids [e.g., *Hamilton et al.*, 1964]. Above NNO + 1, magnetite coexists with all major phases except olivine (Table 7). Proportions of magnetite present are approximately twice higher at ΔNNO > 2.5 than between +1 < ΔNNO < +1.5. Olivine displays a very restricted near-liquidus stability field in the T-f_{O2}-H_2O melt space for the studied basaltic andesite composition. Previous experimental studies on a suite of Grenada samples [*Cawthorn et al.*, 1973; *Graham*, 1981] have shown that at NNO, olivine is no longer the liquidus phase in hydrous mafic melts with MgO < 4–5 wt %. Olivine crystallized in this study is Fo_{69} (Table 8), within the range of olivines in mafic enclaves (Fo_{65-77}), but less Fo-rich than olivines in ash-and-scoria flows (Fo_{71-80}, from *Bourdier et al.*

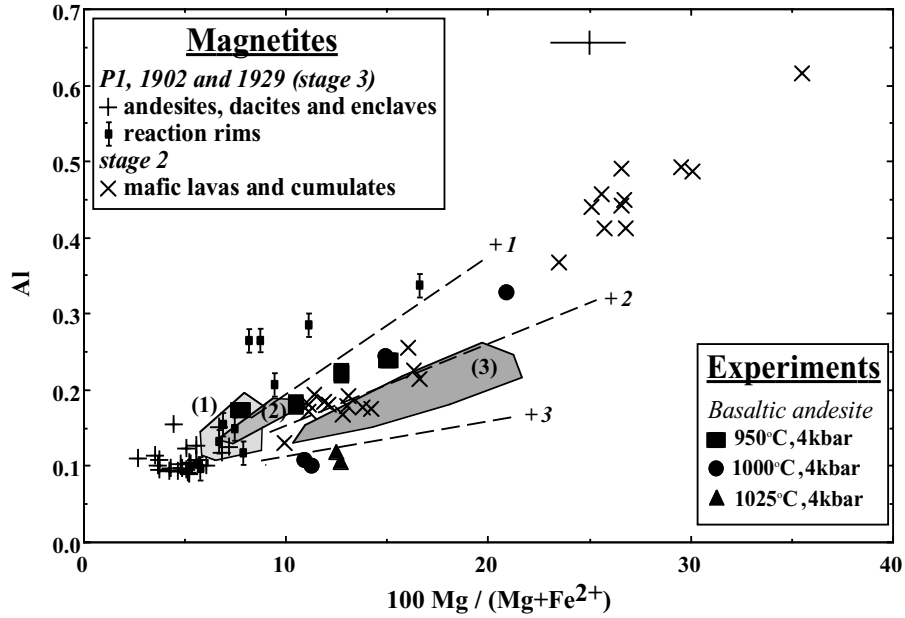

Figure 13. Compositions of experimental magnetites and comparison with natural magnetites from stage 2 and 3 eruption products. Structural formulae are calculated on a 4 oxygen basis. Data are from Table 8 for the basaltic andesite experiments, with charges grouped as in Figure 8. Each experimental data point represents the average composition of magnetite in a given charge. Charges with different f_{O2} are plotted with the same symbol. The three stippled fields show compositions of magnetites in the andesite experiments at 2 kbar [*Martel et al.*, 1999]: (1) 875–900°C, −0.1< ΔNNO < +0.9; (2) 930–950°C, +0.7< ΔNNO < +1.2; and (3) 930–1040°C, +2.0< ΔNNO < +3.2. Dashed lines are ΔNNO contours from data in Table 7. Compositions of natural magnetites are from this study, *Fichaut et al.* [1989a, 1989a], and *Gourgaud et al.* [1989]. Error bar is shown as a cross.

[1985]) and gabbroic cumulates (Fo_{75-81}, from *Fichaut et al.* [1989b]). In the same way, experimental Cpx compositions (Mg # = 60.7–79.6) do not reach the highest values found in mafic lavas (81.4) and cumulates (81.0) [*Bourdier et al.*, 1985; *Fichaut et al.*, 1989b]. This indicates that the starting basaltic andesite is not representative of the most mafic parental liquids present in the chamber.

[41] Experimental results on hydrous mafic melts more primitive than basaltic andesite have shown that below 5 kbar, crystallization of liquidus olivine, clinopyroxene, and spinel generally precedes plagioclase and amphibole [*Holloway and Burnham*, 1972; *Cawthorn et al.*, 1973; *Graham*, 1981; *Sisson and Grove*, 1993a; *Gaetani et al.*, 1993; R, Macdonald and M. Pichavant, manuscript in preparation, 2001]. Consequently, Ol, Cpx, and spinel (Sp) compositions in mafic lavas and cumulates can serve to constrain the composition of the most mafic parental liquids. From the Fe/Mg olivine-melt partition coefficient (0.33, see above), melts coexisting with the most magnesian olivines in gabbroic cumulates (Fo_{75-81}) have Mg # of 49.8–58.5 and with olivines in the mafic lavas (Fo_{71-80}) have Mg # of 44.7–56.9 (for comparison, the Mg # of the starting composition is 48.7, Table 1). The clinopyroxene-melt Fe/Mg partition coefficient yields Mg # of 48.5–56.1 for melts at equilibrium with Cpx from gabbroic cumulates and 39.8–56.7 for Cpx in ash-and-scoria flows (calculations made with $(Fe/Mg)_{Cpx}/(Fe/Mg)_{glass} = 0.3$, see above). The Ol- and Cpx-derived Mg # values overlap, particularly in the high part of the range, suggesting Ol + Cpx cotectic crystallization in the parental mafic liquids. Melt Mg # at equilibrium with magnetites from ash-and-scoria flows and cumulates are in the same range as that inferred from Ol and Cpx compositions, although the results somewhat depend on the magnetite-melt Fe/Mg partition coefficient which is a strong function on f_{O2}. *Fichaut et al.* [1989b] noted that Mt (which may contain up to 2 wt % Cr_2O_3) is an early crystallizing phase in some gabbroic cumulates from Mount Pelée. Interstitial glasses in gabbroic cumulate blocks are basaltic to andesitic [*Bourdier et al.*, 1985; *Fichaut et al.*, 1989b]. The most mafic glass has a Mg # of 52.2, within the range calculated above from Ol and Cpx compositions. It is concluded that the mafic part of the Mount Pelée magma chamber is fed with basaltic parental liquids (Mg # ∼ 55–60). Their crystallization produces a range of derivative liquids from basalt to basaltic andesite (Mg # ∼ 45–50) at equilibrium with Ol + Cpx ± Mt. It is worth emphasizing that basalts with Mg # of ∼55–60 can not be taken as primary mantle melts [*Tatsumi and Eggins*, 1995]. Therefore parental liquids in the mafic part of the Mount Pelée chamber are themselves products of earlier stages of fractionation from more primitive melts at lower crustal or upper mantle depths. Barometric estimates for the Lesser Antilles gabbroic cumulates have yielded pressures between 4 and 10 kbar [*Arculus and Wills*, 1980], suggesting that crystallization of mafic liquids occurs over a substantial pressure range and that the experimental pressure of 4 kbar is appropriate to simulate crystallization processes in the shallowest part of the mafic magma column.

5.2.2. Amphibole stage. [42] The phase assemblage in charge HAB7 (Table 7) illustrates that amphibole may start to crystallize together with olivine and clinopyroxene, as found in some mafic enclaves and gabbroic cumulates [*Lewis*, 1973; *Arculus and Wills*, 1980; *Graham*, 1981; *Fichaut et al.*, 1989b; *Gourgaud et al.*, 1989]. Amphibole crystallization leads to marked changes in phase assemblages, in proportions, and in the composition of coexisting liquids (Tables 7 and 8). Therefore the appearance of amphibole probably corresponds to a major physical and chemical boundary in the mafic part of the chamber. Clinopyroxene and olivine [see *Sisson and Grove*, 1993a] are in reaction relationships with the liquid when amphibole crystallizes. The least magnesian Ol and Cpx in ash-and-scoria flows and gabbroic cumulates coexist at equilibrium with basaltic andesite liquids (Mg # ∼ 45, see above). It is recalled that olivine is barely

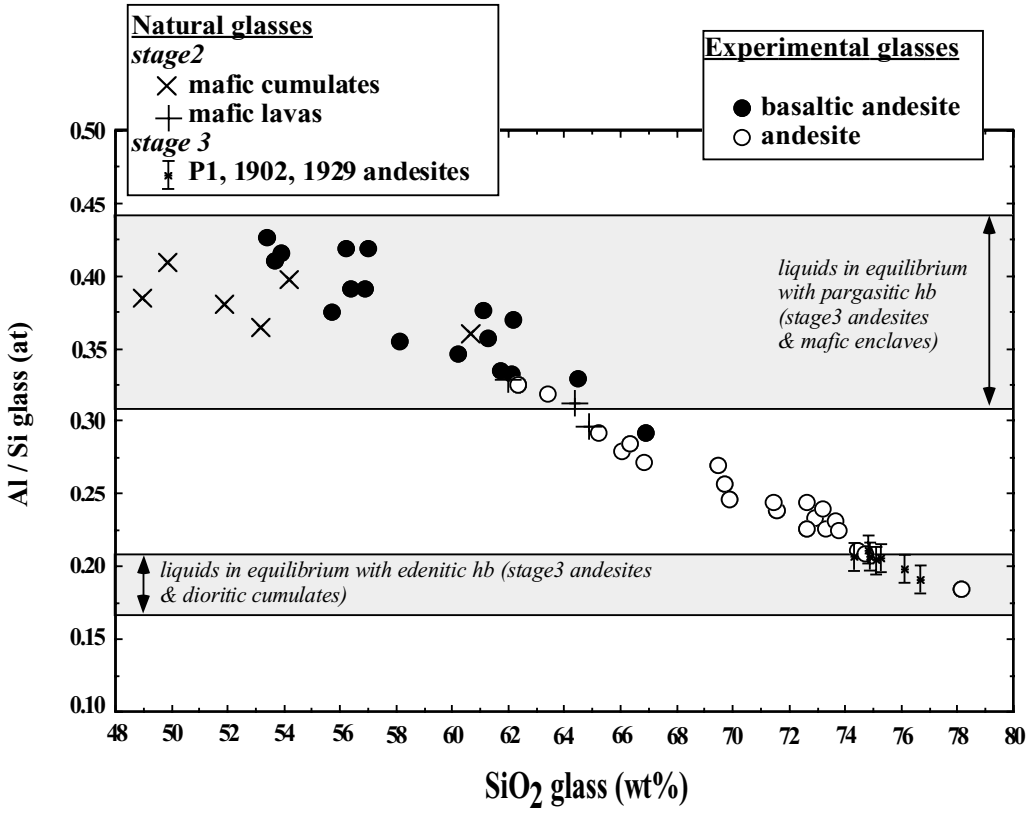

Figure 14. Al/Si (atomic) versus SiO_2 for experimental and natural glasses, normalized to 100% anhydrous. Compositions of experimental glasses from this study (Table 8) for the basaltic andesite experiments and from *Martel et al.* [1999] for the andesite experiments. Note that experiments with different temperatures and f_{O2} are plotted with the same symbol. Compositions of mafic glasses in mafic cumulates and lavas (all stage 2 products) from *Bourdier et al.* [1985] and *Fichaut et al.* [1989a, 1989b] and compositions of interstitial glasses from recent eruptions from this study (Table 6). Compositions (Al/Si) of glasses at equilibrium with pargasitic and edenitic hornblendes from stage 3 products (stippled fields) are calculated with $(Al/Si)_{Amph}/(Al/Si)_{glass} = 0.97$. Error bars are the same size as the symbols.

stable for the basaltic andesite composition studied here and totally absent from the andesite experiments [*Martel et al.*, 1999]. Some Cpx from ash-and-scoria flows indicate crystallization from more evolved (andesitic) liquid compositions, but these may represent phenocrysts derived from andesite during magma mixing [*Bourdier et al.*, 1985]. Similarly, the least magnesian olivines (Fo_{65}) in the mafic enclaves may correspond to Fe-enriched compositions. Olivines with Fo < 65, as observed in some andesites (e.g., Fo_{62}, Table 3) are clearly reacted crystals, as indicated by their relict habits. Therefore mafic products generally lack Ol and Cpx compositions appropriate for crystallization from melts more evolved than basaltic andesite, consistent with the progressive disappearance of Ol and Cpx by reaction with the melt to form amphibole.

[43] At 950°C and for H_2O in melt >5 wt % (Figure 7) the phase assemblage is Plag + Amph ± Mt, depending on f_{O2}. Under these conditions, amphibole is the most abundant phase, exceeding plagioclase in the mineral assemblage (Table 7; see also *Holloway and Burnham* [1972]). This reproduces one important aspect of mafic enclaves and gabbroic cumulates from the Lesser Antilles arc, namely, the high modal abundance of amphibole [*Arculus and Wills*, 1980; *Coulon et al.*, 1984; *Fichaut et al.*, 1989b; *Gourgaud et al.*, 1989]. It has been suggested that fractionation of a Plag + Amph assemblage is responsible for the chemical trends seen in Lesser Antilles lavas [*Arculus and Wills*, 1980]. Compositions of liquids coexisting with amphibole-bearing assemblages range from ~56 at 1000°C to 61–64.5 wt % SiO_2 at 950°C (Table 8 and Figure 9). Amphibole crystallization is therefore associated with a large increase in the SiO_2 content of the coexisting melt. Note that magnetite crystallization has a similar effect. However, charge HAB21 (Tables 7 and 8) shows that high proportions of magnetite (therefore a very high f_{O2}; see Table 7) and high degrees of crystallization are necessary to produce dacitic melt compositions by equilibrium crystallization of an amphibole-free assemblage.

[44] Amphiboles from ash-and-scoria flows and gabbroic cumulates from stage 2 have the most "primitive" chemical characteristics. They define a group with higher Al(IV), number of cations in site A and Mg # than pargasitic amphiboles from recent products, although the two populations partially overlap (Figure 11). The range of coexisting melt Mg # (calculated with $(Fe/Mg)_{Amph}/(Fe/Mg)_{glass} = 0.36$, see above) is 42–55, but most values lie between 50 and 52. Melt Al/Si ratios (calculated with an Al/Si partition coefficient of 0.97, see above) range between 0.38 and 0.49, with most values between 0.44 and 0.48. Therefore both the Fe/Mg and Al/Si ratios of amphiboles in stage 2 mafic products suggest that they crystallized from basaltic to basaltic andesite liquids (e.g., Figure 14 and see *Cawthorn et al.* [1973], *Cawthorn and O'Hara* [1976], *Arculus and Wills* [1980], and *Graham* [1981]). Mg # values derived from amphibole compositions are lower than those calculated from the most magnesian Ol and Cpx (Mg # = 55–60), confirming that amphibole is not quite as early phase to crystallize in parental mafic liquids as Ol + Cpx. However, the stage 2 mafic products provide evidence that amphibole crystallization may have started relatively early. Com-

positions of these natural amphiboles have not been experimentally reproduced in this study, and they would presumably require bulk compositions with higher Al/Si and lower Fe/Mg than the starting basaltic andesite [*Sisson and Grove*, 1993a]. In comparison, amphiboles in the basaltic andesite experiments do have compositions closely matching that of pargasitic hornblende phenocrysts in mafic enclaves and andesites from recent eruptions (Figure 11). Al/Si ratios show that the natural pargasitic hornblendes in recent products crystallized at equilibrium with melts of Al/Si between 0.31 and 0.44, which corresponds to basaltic andesite to dacite liquids (Figure 14). Their Fe/Mg ratios are at equilibrium with slightly less mafic liquids (andesitic to dacitic, Mg # between 31 and 39), close to the 950°C experimental glasses (Table 8). Therefore amphibole was a stable phase in the mafic part of the Mount Pelée chamber, crystallizing at equilibrium with a wide range of melt compositions from basalt to dacite, if compositions of pargasitic hornblende from stage 2 and 3 products are integrated.

5.2.3. T-H_2O melt conditions. [45] Temperatures of parental mafic liquids were calculated using the olivine-liquid and all-liquid thermometers of *Sisson and Grove* [1993b], at a constant pressure of 4 kbar and taking the melt H_2O content as a parameter. Both thermometers slightly underestimate our experimental temperatures by 15–20°C. Compositions of the starting basaltic andesite and of the most mafic basaltic enclave from the 8 May 1902 surge (Mg # = 51.5 [*Gourgaud et al.*, 1989]; see Figure 2) were taken as samples of the most mafic liquids. They coexist with Fo_{74} and $Fo_{75.5}$ olivines, respectively. For 6 wt % H_2O in the melt, calculated olivine-liquid temperatures are 1015°C and 1039°C for the two examples above and 989°C and 1012°C for 8 wt % H_2O. The all-liquid thermometer yields 1011°C and 1026°C for 6 wt % H_2O in the melt. For higher melt H_2O concentrations, results rapidly drop well below experimental liquidus temperatures, suggesting that the all-liquid thermometer [*Sisson and Grove*, 1993b] overestimates the effect of dissolved H_2O above 6 wt %. Nevertheless, the two geothermometers intersect for 1017°C/5.8 wt % H_2O and 1048°C/5.3 wt % H_2O, respectively, for the two examples considered. Considering the errors involved in the calculations and the uncertainties on liquid compositions, we take 1050°C as the average temperature of parental mafic liquids. Temperatures slightly above 1050°C are expected for liquids at equilibrium with the most magnesian olivines from stage 2 products (Fo_{81}).

[46] There are several lines of evidence suggesting H_2O concentrations >5 wt % in the mafic magmas beneath Mount Pelée. In addition to olivine-liquid thermometry the early crystallization of amphibole in the parental mafic liquids requires elevated melt H_2O concentrations, >6 wt % (Figure 7). The high CaO contents of clinopyroxenes from stage 2 [*Bourdier et al.*, 1985] are consistent with crystallization from melts with elevated melt H_2O contents [*Gaetani et al.*, 1993]. Experimental plagioclases do reproduce the compositions of the calcic cores found in mafic enclaves and andesites from stage 3 but only for melt H_2O contents >5–6 wt % (Figure 10). However, the most calcic compositions (An_{94-95} from mafic enclaves, gabbroic cumulates, and ash-and scoria flows) have not been reproduced in the present experiments.

[47] There is also evidence against H_2O-poor mafic magma compositions. The order of appearance of orthopyroxene in the crystallization sequence is strongly dependent on the melt H_2O content. For Opx to crystallize near the liquidus, <5 wt % H_2O are needed (Figure 7). For melt H_2O contents >6–7 wt %, Opx is not stable (Figure 7), in agreement with other studies on hydrous basaltic melts at NNO [*Sisson and Grove*, 1993a]. It is worth pointing out here that Opx is generally absent in the gabbroic cumulates [*Lewis*, 1973; *Fichaut et al.*, 1989b]. From the Opx-melt Fe/Mg partition coefficient, orthopyroxenes in mafic enclaves, lavas, and cumulates crystallized at equilibrium with liquids having Mg # ranging from 39.9 to 21.5. The evolved character of these melts demonstrates that Opx is a late phase and, in fact, the latest in the crystallization sequence of the mafic magmas, which therefore indicates H_2O concentrations >5–6 wt % in the mafic liquids. If melt H_2O contents were lower, then Opx would be both earlier and systematically present in mafic products.

5.2.4. Redox conditions. [48] Compositions of clinopyroxenes in the basaltic andesite experiments are distinctly Al- and Fe^{3+}-rich, identical to salites and augites from lavas and cumulates from stage 2 (Figure 12). In contrast, the few clinopyroxene analyses available for mafic enclaves are Al- and Fe^{3+}-poor and most probably correspond to compositions reequilibrated with host andesite during magma mixing [*Coulon et al.*, 1984; *Gourgaud et al.*, 1989]. Proportions of Fe^{3+} increase along with f_{O2} for both the experimental and the natural Cpx from stage 2 (Figure 12). Wet chemical analyses of mineral separates from gabbroic cumulates from Soufrière, St. Vincent [*Lewis*, 1973], and Mount Pelée (J. Lussigny, unpublished data, 2000) have yielded proportions of Fe^{3+} in the same range as the electron microprobe estimates. By comparison with experimental compositions the proportions of Fe^{3+} in natural clinopyroxene indicate ΔNNO values between <+1 and as high as >+3 for the mafic part of the Mount Pelée magma chamber (Figure 12). Analoguous plots for amphibole (Figure 11) and orthopyroxene (not shown) both indicate ΔNNO between +1 and ≥+2. Although most magnetites from mafic enclaves appear to have reequilibrated, those from mafic lavas and gabbroic cumulates suggest crystallization between ΔNNO > +1 and < +3 (Figure 13).

5.2.5. Summary. [49] Relatively evolved basaltic liquids feed the mafic part of the Mount Pelée magma chamber. They have low temperatures (mostly ≤1050°C), high melt H_2O contents (>5–6 wt %), and high f_{O2} (mostly between 1 and 2 log units above the NNO buffer). Crystallization of these liquids yields early Ol + Cpx + Mt, followed upon decreasing temperature by assemblages dominated by Plag + Amph, although there is evidence that amphibole crystallization may have started early, together with Ol and Cpx. Plag crystallized under these conditions are highly calcic, Cpx are Al- and Fe^{3+}-rich salites, and Amph are pargasitic hornblendes. The experiments reproduce the phenocryst compositions of mafic products from stages 2 and 3, suggesting that they effectively simulate crystallization in the mafic part of the chamber. Recent andesites also carry minor amounts of calcic Plag, Ol, pargasitic Amph, Al-rich Cpx, and aluminous Mt, which therefore must be regarded as crystallization products of mafic magmas.

5.3. Origin of Mafic and Andesitic Magmas

5.3.1. Mafic magmas. [50] The nonprimitive character of the mafic magmas sampled by the eruptions of Mount Pelée represents an unfavorable situation for discussing their origin. More primitive, near-primary high MgO-basalts erupt from other volcanic centers of the central part of the Lesser Antilles arc, such as Soufrière, St. Vincent. These magmas are generated by partial melting from a mantle wedge similar to, or slightly enriched in, high field strength elements (HFSE) relative to the mid-ocean ridge basalt (MORB) source and metasomatized by addition of a fluid phase from the subducting slab [*Heath et al.*, 1998; *Macdonald et al.*, 2000]. Following their emplacement in the upper mantle/deep crust, they fractionate to yield lower-MgO basalts, high-alumina basalts, and basaltic andesites [e.g., *Sisson and Grove*, 1993b] that are dominant in the present-day activity of Soufrière [*Heath et al.*, 1998] and are similar to the mafic liquids feeding the lower part of the Mount Pelée magma chamber. Melt H_2O concentrations as high as 6–8 wt % have been inferred for several low-MgO, high-alumina basalts [*Sisson and Grove*, 1993b; *Sisson and Layne*, 1993; *Roggensack et al.*, 1997], and results presented here provide additional support for H_2O concentrations >5–6 wt % in evolved subduction zone mafic melts. The elevated f_{O2} inferred for the Mount Pelée mafic liquids (≫NNO) is

consistent with the general concept that subduction zone basalts are oxidized.

5.3.2. Andesitic magmas. [51] The origin of silicic compositions in zoned magmatic systems is a controversial subject that has important practical implications for models of zoned magma chambers [e.g., *Hildreth*, 1981; *Eichelberger et al.*, 2000]. At Mount Pelée, previous studies have stressed the importance of crystal fractionation and magma mixing as mechanisms for the origin of the andesitic compositions [*Dupuy et al.*, 1985; *Fichaut et al.*, 1989a; *Smith and Roobol*, 1990]. Magma mixing is unequivocable, as shown, for example, by the occurrence of mafic enclaves in recent products [*Gourgaud et al.*, 1989]. However, several interrelated lines of evidence suggest that the main process responsible for the chemical diversity at Mount Pelée, also essential for the genesis of the andesitic part, is crystal fractionation of basaltic magmas [e.g., *Gill*, 1981].

1. The presence of gabbroic cumulates demonstrates that crystallization of mafic magmas effectively takes place in the chamber. In this process a range of derivative liquids, from basalt to basaltic andesite and from basaltic andesite to dacite once amphibole is fractionating, is generated. Interstitial glasses in gabbroic cumulates record liquid compositions from basalt to andesite, and matrix glasses in mafic stage 2 ash-and-scoria flows are andesitic to dacitic (Figures 10 and 14). Experimental liquids at equilibrium with gabbroic mineral assemblages form a continuous range of compositions from basaltic andesite to dacite, which both mimic and complement the scarce compositions of natural mafic glasses available (Figures 10 and 14).

2. Mineral phase assemblages and compositions in mafic products from stages 2 and 3 are consistent with progressive crystallization of basaltic magmas in the mafic part of the chamber. In particular, amphibole Al/Si and Fe/Mg ratios, which are sensitive indicators of the composition of the coexisting liquid, record a continuous evolution from basaltic-basaltic andesite (pargasitic hornblendes in stage 2 mafic products) to basaltic andesite-dacite (pargasitic hornblendes in stage 3 andesites and mafic enclaves) liquids (Figure 14). About 40% crystallization (in weight) is needed to generate a melt with SiO_2 >60 wt % from a basaltic andesite melt (Table 7).

3. The phase assemblage at equilibrium with derivative liquids of andesitic-dacitic composition is dominated by calcic Plag + Amph (pargasitic hornblende) ± Mt. These phases, together with Al- and Fe^{3+}-rich Cpx and Ol, are also found as rare phenocrysts in recent andesites and mafic enclaves, and their presence stresses the genetic link between andesites and crystallization of basaltic magmas [*Stewart*, 1975].

[52] It is emphasized that the generation of evolved liquid compositions (andesite-dacite) by crystallization of basaltic magmas represents only one step in the origin of andesitic magmas. At Mount Pelée, andesites erupted during the recent period are crystal-rich (35–58 vol %, see above) and contain inherited phenocrysts, and some bear evidence for mixing with mafic magmas represented by the mafic enclaves (in the average proportion of 90:10 [*Gourgaud et al.*, 1989]). Therefore crystallization, mixing, and discharge (eruption) are additional processes to take into consideration when discussing the origin of the Mount Pelée andesites. There is also no indication that the andesite part of the chamber was filled by a single batch of magma, and multiple stages of replenishment involving magma batches slightly differing in composition, crystal content, and temperature need to be considered.

5.4. Model of Magma Chamber

[53] Models of the magma chamber have been discussed previously for Mount Pelée [*Gourgaud et al.*, 1989; *Fichaut et al.*, 1989a; *Smith and Roobol*, 1990]. Critical aspects considered in all models include the well-centered volcanic activity and the small volumes of eruptions, in the 0.1–0.5 km^3 range for the recent period and 1–2 km^3 for stage 2. This has led to the proposal of a funnel-shaped geometry for the magma chamber [*Gourgaud et al.*, 1989; *Fichaut et al.*, 1989a]. To explain the range of magma compositions, the predominance of mafic compositions during stage 2, and the change in erupted magma compositions to mostly andesite during stage 3, earlier models have suggested that the geometry of the magma body evolved from a single physically continuous reservoir during stage 2 [e.g., *Bacon*, 1986] to a physically discontinuous reservoir during stage 3 [*Gourgaud et al.*, 1989; *Fichaut et al.*, 1989a].

[54] A new description of the Mount Pelée magma chamber is proposed in Figure 15. The density and viscosity calculations that support the model are given on Table 9. The main conceptual difference with previous models lies in the coupling between the mafic and the andesitic parts, that is, between crystallization in the mafic part and generation of an andesitic-dacitic liquid which subsequently evolves to produce the andesitic part (see *Druitt and Bacon* [1989] for a similar mechanism in the case of a larger chamber, i.e., Mount Mazama). Hydrous basaltic magmas ascending from lower crustal or upper mantle depths progressively crystallize as a result of the combined effect of (1) elevated magmatic H_2O contents (≥5–6 wt %), which leads to vertical or negative anhydrous mineral saturation curves in P-T space and (2) heat loss that takes place preferentially through the ''head'' of the mafic magma column with a funnel-type geometry as in Figure 15. Crystallization of mafic liquids probably occurs over a substantial pressure range (4–10 kbar [*Arculus and Wills*, 1980]). Derivative liquids ranging from basalt to basaltic andesite are produced at equilibrium with an Ol + Cpx + Mt gabbroic mineral assemblage from ∼1050°C and below (see above). Amphibole joins the gabbroic phase assemblage when temperature falls below ∼1000°C and liquids begin to evolve toward more silicic compositions (andesite to dacite). With progressive crystallization the density of the mafic magmas increases (∼2.5 g cm^{-3}, Table 9), preventing their ascent at shallower levels (limited to ∼3 kbar in Figure 15). The SiO_2-rich residual liquid has a lower density (2.2–2.3 g cm^{-3}, Table 9), and mechanical separation between a dense crystal-rich mush (mafic cumulates) and a buoyant residual melt may take place. Progressive addition of fresh mafic magmas leads to more cumulates in the lower part and accumulation of andesitic-dacitic melts in the upper part of the chamber. Mass balance considerations (see above and Table 7) dictate that residual liquid and gabbroic cumulates coexist in the chamber in a proportion of 60:40 (in wt %) or, more likely, of 50:50 because parental liquids are more mafic than the basaltic andesite starting composition. Assuming that parental mafic compositions have >5–6 wt % H_2O (see above), percentages of crystallization in this range imply conditions near or above H_2O saturation for the derivative liquids for pressures <∼4–5 kbar. Consequently, a free fluid phase probably exists in the shallowest part of the mafic magma column, especially considering that volatile components such as S and C are likely to be present. Andesitic-dacitic magmas ascending from the mafic part of the chamber may carry entrained phenocrysts of dominantly An-rich Plag and pargasitic hornblende, plus minor Ol and Al-rich Cpx. Amphibole resorption will be initiated if the P-T trajectory followed by the andesitic-dacitic magmas upon ascent crosses the amphibole stability curve [*Stewart*, 1975]. Part of the population of An-rich Plag and pargasitic hornblende seen in andesites may also come from the disaggregation of mafic enclaves at shallow levels. Therefore pargasitic amphiboles with different residence times in the andesitic upper part may coexist, explaining why reacted and unreacted amphiboles are found together. Upon ascent and decompression the H_2O content of the melt decreases. Crystallization of an andesitic phase assemblage (Plag + Opx + Mt) may start during ascent and continue once the andesitic-dacitic magmas begin to lose heat in the shallowest part of the chamber (Figures 15c and 15d). With progressive crystallization, residual liquids evolve toward rhyolitic compositions while magma density and viscosity increases (Table 9).

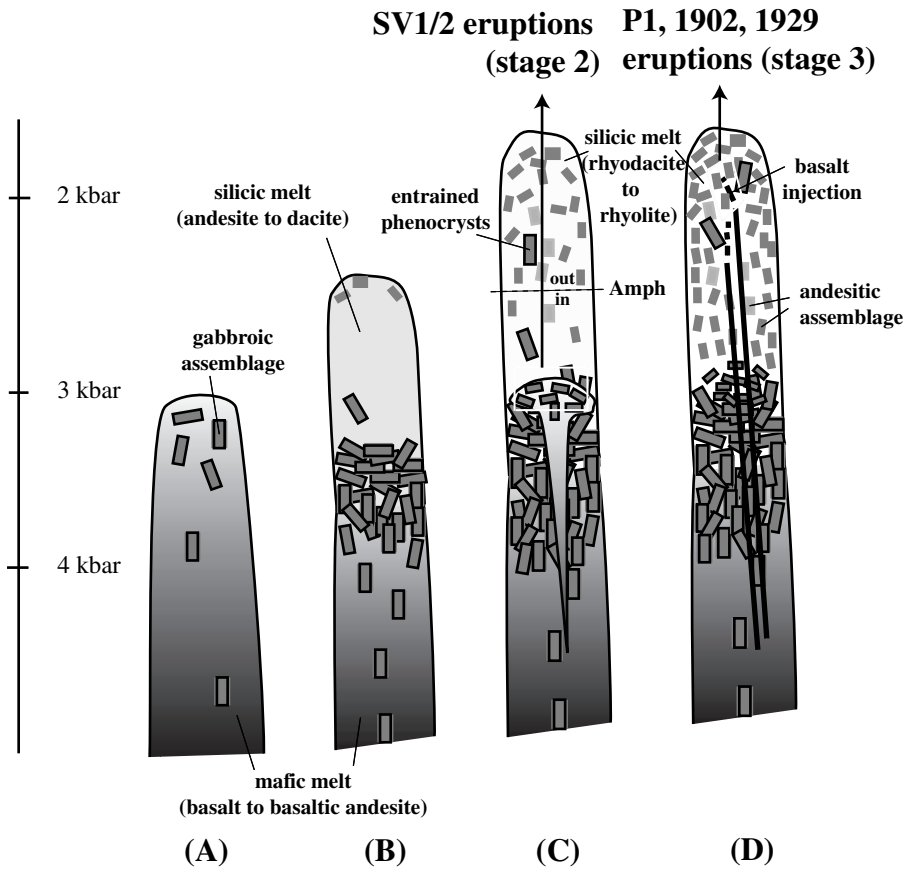

Figure 15. Schematic description of (a,b) the development and activity of the Mount Pelée magma chamber under a regime of (c) high and (d) low flux of mafic magmas. See text. See color version of this figure at back of this issue.

[55] The flux of mafic magmas is considered to be the main parameter governing the activity of the chamber. Important variations of this flux are recorded in the eruptive history of Mount Pelée in the last 40,000 years, and two end-member cases may be illustrated. First, if the flux of mafic magmas is high, the lower part of the chamber may receive frequent additions of large batches of mafic magmas, contributing both heat and mass to the overlying andesitic part. At the same time, basaltic magmas may be injected at shallower levels to form mafic enclaves. Such a regime of activity of the chamber may yield predominantly mafic eruption products, as during stage 2. Marked compositional variations characterize the stage 2 deposits [*Bourdier et al.*, 1985], reflecting tapping of a sharply zoned magma body. These eruptions may have been triggered by mixing between a large body of mafic magma and overlying andesites relatively deep in the chamber (Figure 15c). Andesites from these deposits have bulk compositions nearly identical to those in the recent period, yet they contain 25 vol % phenocrysts [*Bourdier et al.*, 1985], i.e., are much less crystal-rich than recently erupted products (35–58 vol %). Their edenitic amphiboles indicate crystallization at equilibrium with a rhyodacitic melt composition (see above), less silicic than the interstitial melt in present-day andesites. From experiments on the andesite bulk compositions [*Martel et al.*, 1999], these characteristics are consistent with tapping of an andesitic magma body slightly hotter

Table 9. Density and Viscosity Calculations

Magma Composition	Melt Composition	Crystal Content, wt %	T,°C	P, kbar	H_2O Melt, wt %	d,[a] g cm^{-3}	log η,[b] Pa s
Basaltic andesite[c]	basaltic andesite[c]	0	1050	4	6–8	2.38–2.30	0.90–0.41
Basaltic andesite[c]	andesite[d]	36[e]	950	4	6–8	2.58–2.52	2.95–2.27
Andesite[d]	andesite[d]	0	950	4	6–8	2.32–2.25	2.26–1.59
Andesite	rhyolite[f]	50[g]	875	2	5.5–6.5	2.51–2.49	5.27–4.76
Rhyolite[f]	rhyolite[f]	0	875	2	5.5–6.5	2.21–2.18	3.87–3.36

[a] Magma density, with melt density calculated after *Ochs and Lange* [1999].
[b] Melt viscosity calculated after *Shaw* [1972]. For magma viscosity, the Einstein-Roscoe equation has been used [*Scaillet et al.*, 2000].
[c] Experimental glass, HAB0, Table 8.
[d] Experimental glass, HAB11, Table 8.
[e] Density of crystals (gabbroic cumulate assemblage) estimated to 3.2 g cm^{-3}.
[f] Matrix glass, surge, Table 6.
[g] Density of crystals (andesite phenocryst assemblage) estimated to 2.9 g cm^{-3}.

(900–925°C), deeper (2.5 ± 0.5 kbar), and with higher melt H_2O contents (~7 wt %) than during the recent period. Second, if the flux of mafic magmas is low, the lower part of the chamber will receive less heat and mass. Mafic magmas may continue to be added to the upper part, however, but in low and localized amounts, as reflected for example by the few mafic enclaves and hybrid rocks in 1902 and 1929 products (Figure 15d). Injection of mafic magmas provides the thermal energy to balance heat loss and to prevent total solidification of the andesitic crystal-rich mush. The combination of a layer of mafic cumulates below an andesitic crystal-rich mush in the middle part of the chamber (Figure 15d) may act as a physical barrier preventing communication between with the lower and upper parts of the chamber, further restricting access of mafic magmas to higher levels. This regime of activity will be marked by predominantly andesitic eruption products, such as during the present-day. Eruptions such as P6 and P3 (4600 and 2000 years B.P., respectively [*Westercamp and Traineau*, 1983a, *Westercamp and Traineau*, 1983b; Fichaut et al., 1989]), which are characterized by relatively mafic compositions in comparison with the average for stage 3, might correspond to the last major thermal and compositional perturbations (replenishment?) of the andesitic part of the chamber. More recent eruptions (P1, 1902, and 1929) probably tap the same magma body. The stability of P-T-f_{O2}-H_2O melt conditions inferred above for the andesitic part and the lack of evidence for thermal perturbations and reheating indicate balance between the present-day flux of mafic magma and heat loss.

[56] The preceding sections highlight the importance of mafic magmas in the evolution of the Mount Pelée magma chamber. It is tempting to conclude that mafic magmas may also play a role in the triggering of eruptions [*Sparks et al.*, 1977; *Gourgaud et al.*, 1989; *Pallister et al.*, 1996]. However, there is little hint in recent eruption products of significant effects (either thermal or compositional) caused by the intrusion of mafic magmas. This may indicate that the effect of mafic magmas is dominantly mechanical.

6. Conclusions

1. During the last 40,000 years, corresponding to the two last stages of activity of Mount Pelée (stages 2 and 3), mafic magmas have been present among eruption products either as lavas, cumulates, or mafic enclaves, even if the most recently erupted compositions are all andesitic. The magma storage zone beneath Mount Pelée must be viewed as a compositionally zoned igneous body.

2. Preeruptive conditions are identical for the andesitic magma body tapped by the P1, 1902, and 1929 eruptions (875–900°C, 2 ± 0.5 kbar, ΔNNO = +0.4–0.8, melt H_2O content of 5.3–6.3 wt %). These conditions are close to but outside the stability field of amphibole. Experiments on Mount Pelée andesites demonstrate the presence in recent eruption products of a population of crystals (calcic Plag, Ol, pargasitic Amph, Al-rich Cpx, aluminous Mt) out of equilibrium with the andesite magma.

3. Experimental results on a mafic basaltic andesite at 4 kbar demonstrate that the mafic part of the Mount Pelée chamber is fed by relatively evolved basaltic liquids (Mg # ~ 55–60). They have low temperatures (≤1050°C), high melt H_2O contents (>5–6 wt %), and high f_{O2} (mostly between 1 and 2 log units above the NNO buffer). Crystallization of these liquids yields early Ol + Cpx + Mt, followed upon decreasing temperature by assemblages dominated by Plag + Amph, although there is evidence that amphibole crystallization may have started early, together with Ol and Cpx. Plag crystallized under these conditions are highly calcic, Cpx are Al- and Fe^{3+}-rich salites, and Amph are pargasitic hornblendes, reproducing the compositions of phenocryst in mafic lavas and cumulates from stage 2 and in mafic enclaves from stage 3.

4. Experimental liquids at equilibrium with mafic mineral assemblages form a continuous range of compositions from basaltic andesite to dacite, which both mimic and complement the scarce compositions of natural mafic glasses available. Al/Si and Fe/Mg ratios of natural amphiboles record a continuous evolution from basaltic-basaltic andesite to basaltic andesite-dacite liquids in the mafic part of the chamber. The main process responsible for the chemical diversity at Mount Pelée, also essential for the genesis of the andesitic part, is crystal fractionation of basaltic magmas.

5. The mafic and the andesitic parts of the Mount Pelée magma chamber are coupled. Crystallization in the mafic part produces an andesitic-dacitic residual liquid which subsequently evolves to produce the andesitic part. The main parameter governing the activity of the chamber is the flux of mafic magma. The present-day situation is typical of low fluxes of mafic magmas in the chamber in comparison with stage 2.

[57] **Acknowledgments.** Part of this paper comes from the Ph.D. thesis of C. Martel and has benefited from discussions with H. Traineau. J. Cotten is thanked for the chemical analysis of the dark scoria from Grand Rivière. R. Champallier and F. Gaillard assisted during collection of the Karl-Fischer and IR data. We acknowledge D. Baker, J. Hammer, C. Bacon, G. Gaetani, C. Coulon, A. Gourgaud, and M. L. Pascal for their comments and constructive reviews. This study was supported by PNRN.

References

Albarède, F., *Introduction to Geochemical Modelling*, Cambridge Univ. Press, Cambridge, New York, 1995.

Andersen, D. J., D. H. Lindsley, and P. M. Davidson, QUILF: A Pascal program to assess equilibria among Fe-Mg-Ti oxides, pyroxenes, olivine, and quartz, *Comput. Geosci.*, *19*, 1333–1350, 1993.

Arculus, R. J., and K. J. A. Wills, The petrology of plutonic blocks and inclusions from the Lesser Antilles island arc, *J. Petrol.*, *21*, 743–799, 1980.

Bacon, C. R., Magmatic inclusions in silicic and intermediate volcanic rocks, *J. Geophys. Res.*, *91*, 6091–6112, 1986.

Barclay, J., M. J. Rutherford, and R. S. J. Sparks, Experimental phase equilibria constraints on preeruptive storage conditions of the Soufriere Hills magma, *Geophys. Res. Lett.*, *25*, 3437–3440, 1998.

Behrens, H., C. Romano, M. Nowak, F. Holtz, and D. B. Dingwell, Near-infrared determination of water species in glasses of the system $MAlSi_3O_8$ (M = Li, Na, K): an interlaboratory study, *Chem. Geol.*, *128*, 41–63, 1996.

Bellon, H., B. Pelletier, and D. Westercamp, Geochronometric data related to the volcanism of La Martinique, F.W.I., *C. R. Acad. Sci.*, *279*, 457–460, 1974.

Boudon, G., and A. Gourgaud (Eds.), Mount Pelée Special Issue, *J. Volcanol. Geotherm. Res.*, *38*(1–2), 1–213, 1989.

Boudon, G., J.-L. Bourdier, and H. Traineau, High-energy pyroclastic flows in the recent activity of Mt. Pelée, Martinique, paper presented at IAVCEI Congress, Ankara, Turkey, 1994.

Bourdier, J.-L., A. Gourgaud, and P. M. Vincent, Magma mixing in a main stage of formation of Montagne Pelée; the Saint Vincent-type scoria flow sequence (Martinique, FWI), *J. Volcanol. Geotherm. Res.*, *25*, 309–332, 1985.

Bourdier, J.-L., G. Boudon, and A. Gourgaud, Stratigraphy of the 1902 and 1929 nuée-ardente deposits, Mt. Pelée, Martinique, *J. Volcanol. Geotherm. Res.*, *38*(1–2), 77–96, 1989.

Burnham, C. W., The importance of volatile constituents, in *The Evolution of Igneous Rocks*, edited by H. S. Yoder, pp. 439–482, Princeton Univ. Press, Princeton, N. J., 1979.

Cawthorn, R. G., and M. J. O'Hara, Amphibole fractionation in calc-alkaline magma genesis, *Am. J. Sci.*, *276*, 309–329, 1976.

Cawthorn, R. G., E. B. Curran, and R. J. Arculus, A petrogenetic model for the origin of the calk-alkaline suite of Grenada, Lesser Antilles, *J. Petrol.*, *14*, 327–337, 1973.

Chou, I. M., Oxygen buffer and hydrogen sensor technique at elevated pressures and temperature, in *Hydrothermal Experimental Techniques*, edited by H. L. Barnes and G. C. Ulmer, pp. 61–99, John Wiley, New York, 1987.

Clynne, M. A., A complex magma mixing origin for rocks erupted in 1915, Lassen Peak, California, *J. Petrol.*, *40*, 105–132, 1999.

Cotten, J., A. Le Dez, M. Bau, M. Carroff, R. C. Maury, P. Dulski, S. Fourcade, M. Bohn, and R. Brousse, Origin of anomalous rare-earth element and yttrium enrichments in subaerially exposed basalt: Evidence from French Polynesia, *Chem. Geol.*, *119*, 115–138, 1995.

Coulon, C., R. Clocchiatti, R. C. Maury, and D. Westercamp, Petrology of basaltic xenoliths in andesitic to dacitic host lavas from Martinique (Les-

ser Antilles): Evidence for magma mixing, *Bull. Volcanol.*, *47*(4), 705–734, 1984.

Devine, J. D., J. E. Gardner, H. P. Brack, G. D. Layne, and M. J. Rutherford, Comparison of microanalytical methods for estimating H_2O contents of silicic volcanic glasses, *Am. Mineral.*, *80*, 319–328, 1995.

Dixon, J. E., E. M. Stolper, and J. R. Holloway, An experimental study of water and carbon dioxide solubilities in mid-ocean ridge basaltic liquids, part I, Calibration and solubility models, *J. Petrol.*, *36*, 1607–1631, 1995.

Druitt, T. H., and C. R. Bacon, Petrology of the zoned calcalkaline magma chamber of Mount Mazama, Crater Lake, Oregon, *Contrib. Mineral. Petrol.*, *101*, 245–259, 1989.

Dupuy, C., J. Dostal, and H. Traineau, Geochemistry of volcanic rocks from Mt. Pelée, Martinique, *J. Volcanol. Geotherm. Res.*, *26*, 147–165, 1985.

Eichelberger, J. C., and H. R. Westrich, Magmatic volatiles in explosive rhyolitic eruptions, *Geophys. Res. Lett.*, *8*, 757–760, 1981.

Eichelberger, J. C., C. R. Carrigan, H. R. Westrich, and R. H. Price, Non-explosive silicic volcanism, *Nature*, *323*, 598–602, 1986.

Eichelberger, J. C., D. G. Chertkoff, S. T. Dreher, and C. J. Nye, Magmas in collision: rethinking chemical zonation in silicic magmas, *Geology*, *28*, 603–606, 2000.

Fichaut, M., R. C. Maury, H. Traineau, D. Westercamp, J.-L. Joron, A. Gourgaud, and C. Coulon, Magmatology of Mt Pelée (Martinique, F.W.I), III, Fractional crystallisation versus magma mixing, *J. Volcanol. Geotherm. Res.*, *38*(1–2), 189–213, 1989a.

Fichaut, M., G. Marcelot, and R. Clocchiatti, Magmatology of Mt Pelée (Martinique, F.W.I), II, Petrology of gabbroic and dioritic cumulates, *J. Volcanol. Geotherm. Res.*, *38*(1–2), 171–188, 1989b.

Fink, J. H., Structure and emplacement of a rhyolitic obsidian flow: Little Glass Mountain, Medicine Lake Highland, northern California, *Geol. Soc. Am. Bull.*, *94*, 362–380, 1983.

Gaetani, G. A., T. L. Grove, and W. B. Bryan, The influence of water on the petrogenesis of subduction-related igneous rocks, *Nature*, *365*, 332–334, 1993.

Gaillard, F., B. Scaillet, M. Pichavant, and J.-M. Bény, The effect of water and fO_2 on the ferric-ferrous ratio of silicic melts, *Chem. Geol.*, *174*, 255–273, 2001.

Gardner, J. E., Experimental constraints on pre-eruptive water contents and changing magma storage prior to explosive eruptions of Mount St. Helens volcano, *Bull. Volcanol.*, *57*, 1–17, 1995.

Ghiorso, M. S., On the stability relations of hydrous minerals in water-undersaturated magmas, *Am. Mineral.*, *84*, 1506–1511, 1999.

Ghiorso, M. S., and R. O. Sack, Fe-Ti oxide geothermometry: thermodynamic formulation and estimation of intensive variables in silicic magmas, *Contrib. Mineral. Petrol.*, *108*, 485–510, 1991.

Gill, J. B., *Orogenic Andesites and Plate Tectonics*, Springer-Verlag, New York, 1981.

Gourgaud, A., M. Fichaut, and J.-L. Joron, Magmatology of Mt. Pelée (Martinique, F.W.I.), I, Magma mixing and triggering of the 1902 and 1292 Pelean nuées ardentes, *J. Volcanol. Geotherm. Res*, *38*(1–2), 143–169, 1989.

Govindaraju, K., Compilation of working values and sample description for 383 geostandards, *Geostand. News.*, *18*, 158 pp., 1994.

Graham, A. M., Melting relations of island arc lavas from Grenada, Lesser Antilles, *Progress in Exploration Petrology*, *NERC Publ. Ser. D*, vol. 18, edited by C. E. Ford, pp. 126–132, 1981.

Grove, T. L., J. M. Donnelly-Nolan, and T. Housh, Magmatic processes that generated the rhyolite of Glass Mountain, Medicine Lake volcano, N. California, *Contrib. Mineral. Petrol.*, *127*, 205–223, 1997.

Hamilton, D. L., C. W. Burnham, and E. F. Osborn, The solubility of water and effects of oxygen fugacity and water content on crystallization in mafic magmas, *J. Petrol.*, *5*, 21–39, 1964.

Heath, E., R. Macdonald, H. Belkin, C. Hawkesworth, and H. Sigurdsson, Magma genesis at Soufrière volcano, St Vincent, Lesser Antilles arc, *J. Petrol.*, *39*, 1721–1764, 1998.

Hildreth, W., Gradients in silicic magma chambers: Implications for lithospheric magmatism, *J. Geophys. Res.*, *86*, 10,153–10,192, 1981.

Holloway, J. R., The system pargasite-H_2O-CO_2: A model with a mixed-volatile fluid, I, Experimental results to 8 kbar, *Geochim. Cosmochim. Acta*, *37*, 651–666, 1973.

Holloway, J. R., and J. G. Blank, Application of experimental results to C-O-H species in natural melts, in *Volatiles in Magmas*, edited by M. R. Carroll and J. R. Holloway, pp. 187–230, *Mineral. Soc. of Am.*, Washington, D. C., 1994.

Holloway, J. R., and C. W. Burnham, Melting relations of basalt with equilibrium water pressure less than total pressure, *J. Petrol.*, *13*, 1–29, 1972.

Housh, T. B., and J. F. Luhr, Plagioclase-melt equilibria in hydrous systems, *Am. Mineral.*, *76*, 477–492, 1991.

Jaupart, C., and C. J. Allègre, Gas content, eruption rate and instabilities of eruption regime in silicic volcanoes, *Earth Planet. Sci. Lett.*, *102*, 413–429, 1991.

Lacroix, A., *La Montagne Pelée et ses Eruptions*, 662 pp., Masson, Paris, 1904.

Lewis, J. F., Petrology of the ejected plutonic blocks of the Soufrière volcano, St. Vincent, West Indies, *J. Petrol.*, *14*, 81–112, 1973.

Lindsley, D. H., Pyroxene thermometry, *Am. Mineral.*, *68*, 477–493, 1983.

Macdonald, R., C. J. Hawkesworth, and E. Heath, The Lesser Antilles Volcanic chain: a study in arc magmatism, *Earth Sci. Rev.*, *49*, 1–76, 2000.

Martel, C., M. Pichavant, J.-L. Bourdier, H. Traineau, F. Holtz, and B. Scaillet, Magma storage conditions and control of eruption regime in silicic volcanoes: Experimental evidence from Mt. Pelée, *Earth Planet. Sci. Lett.*, *156*, 89–99, 1998.

Martel, C., M. Pichavant, F. Holtz, B. Scaillet, J.-L. Bourdier, and H. Traineau, Effects of fO_2 and H_2O on andesite phase relations between 2 and 4 kbar, *J. Geophys. Res.*, *104*, 29,453–29,470, 1999.

Martel, C., J.-L. Bourdier, M. Pichavant, and H. Traineau, Textures, water content and degassing of silicic andesites from recent plinian and dome-forming eruptions at Mount Pelée volcano (Martinique, Lesser Antilles arc), *J. Volcanol. Geotherm. Res.*, *96*, 191–206, 2000.

Miyashiro, A., Volcanic rock series in island arcs and active continental margins, *Am. J. Sci.*, *283*, 993–1033, 1974.

Nagle, F., J. J. Stipp, and D. E. Fischer, K-Ar geochronology of the Limestones Caribbees and Martinique, Lesser Antilles, West Indies, *Earth Planet. Sci. Lett.*, *29*, 401–412, 1976.

Nakada, S., C. R. Bacon, and A. E. Gartner, Origin of phenocrysts and compositional diversity in pre-Mazama rhyodacitic lavas, Crater Lake, Oregon, *J. Petrol.*, *35*, 127–162, 1994.

Ochs, F. A., and R. A. Lange, The density of hydrous magmatic liquids, *Science*, *283*, 1314–1317, 1999.

Pallister, J. S., R. P. Hoblitt, G. P. Meeker, R. J. Knight, and D. F. Siems, Magma mixing at Mount Pinatubo: petrographic and chemical evidence from the 1991 deposits, in *Fire and Mud, Eruptions and Lahars of Mount Pinatubo, Philippines*, edited by C. G. Newhall and R. S. Punongbayan, pp. 687–731, Univ. of Wash. Press, Seattle, 1996.

Papike, J. J., K. L. Cameron, and K. Baldwin, Amphiboles and pyroxenes: Characterization of other than quadrilateral components and estimates of ferric iron from microprobe data, *Geol. Soc. Am. Abstr. Programs*, *6*, 1053–1054, 1974.

Perret, F. A., The Eruptions of Mt. Pelée 1929-1932, *Carnegie Inst. Washington Publ. 458*, 126 pp., 1937.

Pichavant, M., The effects of boron and water on liquidus phase relations in the haplogranite system at 1 kbar, *Am. Mineral.*, *72*, 1056–1070, 1987.

Roggensack, K., R. L. Hervig, S. B. McKnight, and S. N. Williams, Explosive basaltic volcanism from Cerro Negro volcano: Influence of volatiles on eruptive style, *Science*, *277*, 1639–1642, 1997.

Roobol, M. J., and A. L. Smith, Mount Pelée, Martinique: A pattern of alternating eruptive style, *Geology*, *4*, 521–524, 1976.

Roux, J., and A. Lefèvre, A fast quench device for internally heated pressure vessels, *Eur. J. Mineral.*, *4*, 279–281, 1992.

Rutherford, M. J., and J. D. Devine, The May 18, 1980, eruption of Mount St. Helens, 3, Stability and chemistry of amphibole in the magma chamber, *J. Geophys. Res.*, *93*, 11,949–11,959, 1988.

Rutherford, M. J., and J. D. Devine, Pre-eruption pressure-temperature conditions and volatiles in the 1991 Mount Pinatubo magma, in *Fire and Mud, Eruptions and Lahars of Mount Pinatubo, Philippines*, edited by C. G. Newhall and R. S. Punongbayan, pp. 751–766, Univ. of Wash. Press, Seattle, 1996.

Rutherford, M. J., and P. M. Hill, Magma ascent rates from amphibole breakdown: An experimental study applied to the 1980–1986 Mount St. Helens eruptions, *J. Geophys. Res.*, *98*, 19,667–19,685, 1993.

Rutherford, M. J., H. Sigurdsson, S. Carey, and A. Davis, The May 18, 1980, eruption of Mount St. Helens, 1, Melt composition and experimental phase equilibria, *J. Geophys. Res.*, *90*, 2929–2947, 1985.

Scaillet, B., and B. W. Evans, The 15 June 1991 eruption of Mount Pinatubo, I, Phase equilibria and pre-eruption P-T-fO_2-fH_2O conditions of the dacite magma, *J. Petrol.*, *40*, 381–411, 1999.

Scaillet, B., M. Pichavant, and J. Roux, Experimental crystallization of leucogranite magmas, *J. Petrol.*, *36*, 663–705, 1995.

Scaillet, B., A. Whittington, C. Martel, M. Pichavant, and F. Holtz, Phase equilibrium constraints on the viscosity of silicic magmas, II, Implications for mafic-silicic mixing processes, *Trans. R. Soc. Edinburgh Earth Sci.*, *91*, 61–72, 2000.

Shaw, H. R., Viscosities of magmatic silicate liquids: an empirical method of prediction, *Am. J. Sci.*, *272*, 870–893, 1972.

Sisson, T. W., and T. L. Grove, Experimental investigations of the role of H_2O in calk-alkaline differentiation and subduction zone magmatism, *Contrib. Mineral. Petrol.*, *113*, 143–166, 1993a.

Sisson, T. W., and T. L. Grove, Temperatures and H_2O contents of low-MgO high alumina basalts, *Contrib. Mineral. Petrol.*, *113*, 167–184, 1993b.

Sisson, T. W., and G. D. Layne, H_2O in basalt and basaltic andesite glass inclusions from four subduction-related volcanoes, *Earth Planet. Sci. Lett.*, *117*, 619–635, 1993.

Smith, A. L., and M. J. Roobol, *Mt. Pelée, Martinique, A Study of an Active Island-Arc Volcano*, *Mem. Geol. Soc. Am.*, *175*, 105 pp., 1990.

Sparks, R. S. J., H. Sigurdsson, and L. Wilson, Magma mixing: A mechanism for triggering acid explosive eruptions, *Nature*, *267*, 315–318, 1977.

Stewart, D. C., Crystal clots in calc-alkaline andesites as breakdown products of high-Al amphiboles, *Contrib. Mineral. Petrol.*, *53*, 195–204, 1975.

Tatsumi, Y., and S. Eggins, *Subduction Zone Magmatism*, 211 pp., Blackwell, Malden, Mass., 1995.

Traineau, H., D. Westercamp, J.-M. Bardintzeff, and J.-C. Miskovski, The recent pumice eruptions of Mt. Pelée volcano, Martinique, part I, Depositional sequences, description of pumiceous deposits, *J. Volcanol. Geotherm. Res.*, *38*(1–2), 17–33, 1989.

Villemant, B., and G. Boudon, Transition from dome-forming to plinian eruptive styles controlled by H_2O and Cl degassing, *Nature*, *392*, 65–69, 1998.

Villemant, B., G. Boudon, and J.-C. Komorowski, U-series disequilibrium in arc magmas induced by water-magma interaction, *Earth Planet. Sci. Lett.*, *140*, 259–267, 1996.

Vincent, P. M., J.-L. Bourdier, and G. Boudon, The primitive volcano of Mount Pelée: Its construction and partial destruction by flank collapse, *J. Volcanol. Geotherm. Res.*, *38*(1–2), 1–16, 1989.

Westercamp, D., and H. Traineau, Geological map of Mount Pelée at 1/20 000 scale, Dép. de la Martinique, BRGM, Orléans, France, 1983a.

Westercamp, D., and H. Traineau, The past 5000 years of volcanic activity at Mt. Pelée, Martinique (F.W.I.): Implications for assessement of volcanic hazards, *J. Volcanol. Geotherm. Res.*, *17*, 159–185, 1983b.

J.-L. Bourdier, M. Pichavant, and B. Scaillet, Institut des Sciences de la Terre (ISTO), 1A, rue de la Férollerie, F-45071 Orléans Cedex 02, France. (pichavan@cnrs-orleans.fr)

C. Martel, Bayerisches Geoinstitut, Universität Bayreuth, D-95444 Bayreuth, Germany.

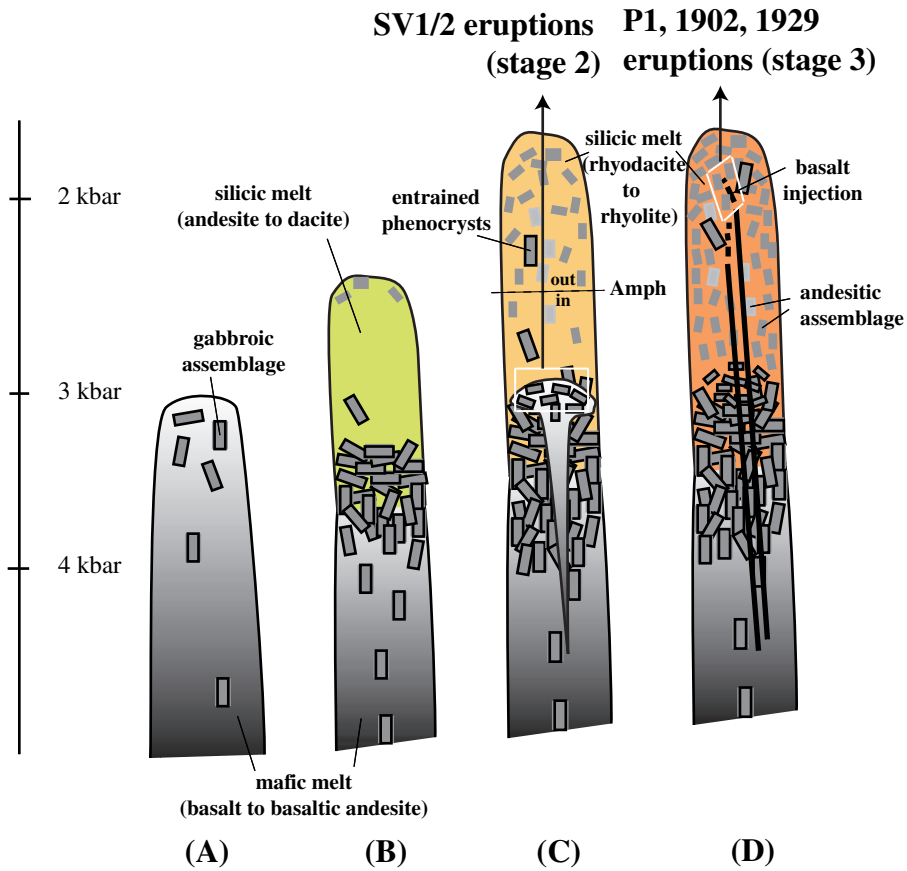

Figure 15. Schematic description of (a,b) the development and activity of the Mount Pelée magma chamber under a regime of (c) high and (d) low flux of mafic magmas. See text.